

Automatic near real-time flood detection using Suomi-NPP/VIIRS data

Sanmei Li^{a,*}, Donglian Sun^a, Mitchell D. Goldberg^b, Bill Sjoberg^b, David Santek^c, Jay P. Hoffman^c, Mike DeWeese^d, Pedro Restrepo^d, Scott Lindsey^e, Eric Holloway^e

^a Department of Geography and Geo-Information Science, George Mason University, Fairfax, VA 22030, USA

^b NOAA JPSS Program Office, Lanham, MD, USA

^c Space Science and Engineering Center, University of Wisconsin-Madison, Madison, WI 53706, USA

^d North Central River Forecast Center, National Weather Service, NOAA, Chanhassen, MN 55317-8581, USA

^e Alaska-Pacific River Forecast Center, National Weather Service, NOAA, Anchorage, AK 99502, USA



Articolo estremamente tecnico,
non usando Deep Learning c'è
un botto di roba di image processing
e concetti legati alla riflessione/rifrazione
della luce a seconda del materiale
intorno/sotto ai corsi d'acqua. Un bordello.

ARTICLE INFO

Keywords:

JPSS

SNPP/VIIRS

Near real-time flood detection

VNG flood V1.0

ABSTRACT

Near real-time satellite-derived flood maps are invaluable to river forecasters and decision-makers for disaster monitoring and relief efforts. With support from the JPSS (Joint Polar Satellite System) Proving Ground and Risk Reduction (PGRR) Program, flood detection software has been developed using Suomi-NPP/VIIRS (Suomi National Polar-orbiting Partnership/Visible Infrared Imaging Radiometer Suite) imagery to automatically generate near real-time flood maps for National Weather Service (NWS) River Forecast Centers (RFC) in the USA. The software, which is called VIIRS NOAA GMU Flood Version 1.0 (hereafter referred to as VNG Flood V1.0), consists of a series of algorithms that include water detection, cloud shadow removal, terrain shadow removal, minor flood detection, water fraction retrieval, and floodwater determination. The software is designed for flood detection in any land region between 80°S and 80°N, and it has been running routinely with direct broadcast SNPP/VIIRS data at the Space Science and Engineering Center at the University of Wisconsin-Madison (UW/SSEC) and the Geographic Information Network of Alaska at the University of Alaska-Fairbanks (UAF/GINA) since 2014. Near real-time flood maps are distributed via the Unidata Local Data Manager (LDM), reviewed by river forecasters in AWIPS-II (the second generation of the Advanced Weather Interactive Processing System) and applied in flood operations. Initial feedback from operational forecasters on the product accuracy and performance has been largely positive. The software capability has also been extended to areas outside of the USA via a case-driven mode to detect major floods all over the world. Offline evaluation efforts include the visual inspection of over 10,000 VIIRS false-color composite images, an inter-comparison with MODIS automatic flood products and a quantitative validation using Landsat imagery. The steady performance from the 3-year routine process and the promising evaluation results indicate that VNG Flood V1.0 has a high feasibility for flood detection at the product level.

1. Introduction

As the costliest natural disasters worldwide, most climate change forecasts predict that floods will become increasingly frequent (Milly et al., 2002; Hirabayashi et al., 2008; Lehner et al., 2006). At high latitudes, floods are caused by ice jams and snow melt during almost every break-up season. Floods caused by intense rainfall also threaten the safety of human lives and property. Near real-time satellite-derived flood maps are invaluable to river forecasters and decision-makers for disaster monitoring and relief efforts.

Flood detection has a history in satellite remote sensing that dates back to the 1970s. Imagery from the NOAA (National Oceanic and Atmospheric Administration) VHRR (Very High Resolution

Radiometer) and AVHRR (Advanced Very High Resolution Radiometer) served as the main data sources for flood/standing water detection prior to the development of the MODIS (Moderate Resolution Imaging Spectroradiometer) system. Many case studies have been conducted to analyze severe flood events all over the world. These studies laid a foundation for the methods and approaches of flood detection with coarse-to-moderate-resolution satellite data (Wiesnet et al., 1974; Barton and Bathols, 1989; Ali, 1989; Sheng and Xiao, 1994; Sheng et al., 1998; Sheng and Gong, 2001). With coarse 1-km spatial resolutions, however, VHRR and AVHRR data could only show the macro flood distributions of select major floods and failed to address any inundation details. To resolve this issue, Landsat imagery with a 30-m spatial resolution is widely used as an alternative in flood detection,

* Corresponding author.

E-mail address: slia@gmu.edu (S. Li).

disaster assessment and flood pattern analysis (Gupta and Bodechtel, 1982; Gupta and Banerji, 1985; Wang et al., 2002; Mueller et al., 2016; Fisher et al., 2016; Tulbure et al., 2016). Although VHRR, AVHRR and Landsat imagery play effective roles in flood mapping, the flood detection capabilities of these optical sensors can be severely affected by cloud cover during flood periods. To derive flood information under cloud cover, radar remote sensing satellites and imaging systems such as Radarsat, SAR, TerraSAR-X and Sentinel-1 are becoming more popular in flood monitoring and analysis. Their high spatial resolution and capability to penetrate cloud cover make radar data very popular in hydrological fields for multiple-scale flood mapping, flood management and disaster relief (Brakenridge et al., 1994; Matgen et al., 2007; Schumann et al., 2007; Martinis et al., 2009; Matgen et al., 2011; Pulvirenti et al., 2011; Martinis et al., 2013).

Although Landsat and radar imagery have excellent capabilities for flood mapping, the narrow swath widths and long revisit periods of their sensors are major drawbacks. Because most floods are short-term events, it is not realistic to completely rely upon these images for flood mapping and management purposes. In comparison, moderate-spatial-resolution satellites provide steadier and lower-cost data sources for near real-time flood mapping. After the EOS (Earth Observing System) flagship Terra was launched in 1999, MODIS has gradually become the preferred satellite instrument for flood detection because of its daily global coverage and higher spatial resolution of the visible, near infrared (250 m) and shortwave infrared (500 m) channels compared to the 1-km resolution channels with the AVHRR (Gumley and King, 1995; Brakenridge and Anderson, 2006). Newer algorithms such as the decision-tree approach and the open water likelihood method have used MODIS to more accurately detect flooding and standing water (Sun et al., 2012; Ticehurst et al., 2014; Ticehurst et al., 2015). The continuous observations from MODIS also make it possible to analyze flood inundation dynamics and generate global water masks from multiple-year detected results (Carroll et al., 2009; Andrimont et al., 2012; Huang et al., 2014). In 2011, an experimental global flood detection system using MODIS imagery was released by NASA (National Aeronautics and Space Administration) (<http://oas.gsfc.nasa.gov/floodmap>). This system processes near real-time MODIS data and generates 1-day, 2-day, 3-day and 14-day composite global flood products for $10^\circ \times 10^\circ$ tiles from the MODIS instrumentation aboard the Terra and Aqua satellites (Brakenridge, 2011). The system also provides systematic datasets with a robust interface to access the products. The multiple-day composition process is applied mainly in order to filter out cloud shadows and terrain shadows, and it produces multiple-day composite flood maps rather than near real-time ones. The problem with the multiple-day composition process is that some real floodwater data may be lost in the composition process, and the process introduces a bias in the experimental MODIS flood maps. Even after the composition process has finished, cloud shadows can persist in the MODIS flood products, especially at high latitudes. More recently, the HAND (height above nearest drainage) algorithm has been applied to MODIS flood detection attempts with a better removal of terrain shadows. The accuracy of MODIS flood products are still susceptible to deep terrain shadows that cannot be filtered either through multiple-day compositions or the HAND algorithm (Brakenridge, 2011; Liu et al., 2016).

With the launch of the Suomi-NPP in 2012, the VIIRS sensor has exhibited many advantages over MODIS data in environmental and natural disaster monitoring and analysis. SNPP/VIIRS imagery has a moderate spatial resolution of 375 m in the shortwave IR bands, a swath coverage width of 3000 km, and a relatively constant resolution across the scan. These new features make SNPP/VIIRS data an excellent source for near real-time flood detection. With the support of the JPSS/PGRR program since 2013, VNG Flood V1.0 has been developed using SNPP/VIIRS imagery to derive near real-time flood maps for the National Weather Service (NWS) River Forecast Centers (RFC) in the USA. A series of algorithms have been developed in the software, including those for water detection, cloud shadow removal, terrain

shadow removal, minor flood detection, water fraction retrieval, and floodwater determination. The successful development of the cloud shadow and terrain shadow removal algorithms promises consistent results and makes the detection of near real-time flooding feasible and operational using moderate-resolution satellite data. This paper presents a comprehensive introduction to the software, describes the required datasets, introduces the algorithms, presents the results, and concludes with a summary discussion.

2. Data used

The main datasets used for flood detection with the VIIRS imagery are the SNPP/VIIRS SDR (sensor data record) data in imager bands 1 (600–680 nm), 2 (850–880 nm), 3 (1610 nm) and 5 (1050–1240 nm) with nominal resolutions of 375 m and 1-band terrain-corrected geolocation data, which includes longitude, latitude, solar zenith angles, solar azimuth angles, sensor zenith angles and sensor azimuth angles (GITCO). The SNPP/VIIRS 750-m resolution cloud mask intermediate product (IICMO) and M-band terrain-corrected geolocation data (GMTCO) are used to help determine the cloud cover. Because VIIRS SDR data and IICMO data are stored in swath granules with an hdf5 format, a module was developed to project the VIIRS swath granules between 80°S and 80°N into an equidistant cylindrical projection based on MS2GT0.24 (<https://nsidc.org/data/modis/ms2gt/index.html>). In addition to the SNPP/VIIRS SDR and EDR (earth data record) datasets, static ancillary datasets are also utilized to assist with water detection and flood determination. These ancillary datasets include global land cover from the IGBP, global land/sea masks, digital elevation models (DEMs) from the SRTM-2 (Shuttle Radar Topography Mission version 2) and ASTER (Advanced Spaceborne Thermal Emission and Reflection Radiometer), MODIS 250-m global water masks (MOD44 W) (Rabus et al., 2003; Tachikawa et al., 2011; Carroll et al., 2009), and water layers from the 2006 30-m National Land Cover Database (Xian et al., 2009).

3. Methods

3.1. Physical basis

Water detection with vegetation and bare land background conditions using optical satellite data is primarily based on the spectral differences between water features and other land cover types in the visible (Vis, VIIRS I1 band: 600–680 nm), near infrared (NIR, VIIRS I2 band: 850–880 nm) and shortwave infrared (SWIR, VIIRS I3 band: 1580–1640 nm) channels (Wiesnet et al., 1974; Barton and Bathols, 1989; Sheng and Xiao, 1994). As shown in Fig. 1, water has a higher reflectance in the Vis channel than in the NIR and SWIR channels. Vegetation is more reflective in the NIR channel than in the Vis channel. The reflectance of bare land increases with increasing wavelengths with a maximum in the SWIR channel, whereas the reflectance of water is close to 0 in the SWIR channel. Based on these spectral characteristics, several variables, including the NDVI (normalized difference vegetation index), NDSI (normalized difference snow index) and NDWI (normalized difference water index), are widely applied for water detection purposes. The NDVI, NDSI and NDWI are defined hereinafter (Rouse et al., 1974; Sellers, 1985; Xiao et al., 2001; Gao, 1996; Ceccato et al., 2002).

$$\text{NDVI} = \frac{R_{\text{NIR}} - R_{\text{Vis}}}{R_{\text{NIR}} + R_{\text{Vis}}} \quad (1)$$

$$\text{NDSI} = \frac{R_{\text{Vis}} - R_{\text{SWIR}}}{R_{\text{Vis}} + R_{\text{SWIR}}} \quad (2)$$

$$\text{NDWI} = \frac{R_{\text{NIR}} - R_{\text{SWIR}}}{R_{\text{NIR}} + R_{\text{SWIR}}} \quad (3)$$

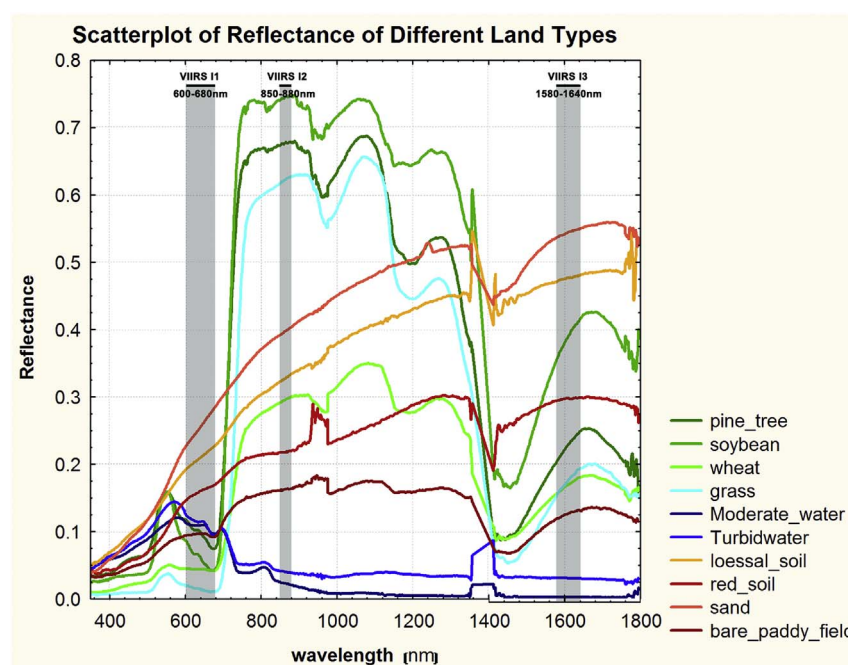


Fig. 1. Plot of reflectance of different land types from VIS to SWIR band range (Zhang et al., 2008).

In Eqs. (1) through (3), R_{VIS} is the reflectance in the Vis channel, R_{NIR} is the reflectance in the NIR channel, and R_{SWIR} is the reflectance in the SWIR channel. These three indices show similar or better discriminatory capabilities in water detection than R_{VIS} , R_{NIR} and R_{SWIR} . However, the three indices are unable to independently differentiate floodwater from other land types. Instead, the combination of these variables forms the basis of a robust flood detection technique.

Unlike water detection with a background of vegetation and bare land, floodwater with a background of snow/ice reflects much more greatly in the Vis and NIR channels due to the mixture of snow/ice signals but retains the features with higher reflectance in the Vis channel more than those in the NIR channel (Liang et al., 2012; Johansson and Brown, 2013; Lesson et al., 2013). The detection of floodwater also depends on similar variables: R_{VIS} , R_{NIR} and NDVI. Melting snow/ice surfaces and shadows that are cast on snow/ice surfaces can be confused with supra-snow/ice water because of similar spectral features in these three variables. To solve this problem, a new DNDVI variable is defined as the NDVI difference between a pixel and the surrounding snow/ice surface. With similar R_{VIS} and R_{NIR} values, a melting snow surface and shadows that are cast on a snow surface have smaller negative DNDVI values than those of supra-snow/ice water. Fig. 2 presents four scatter plots collected from approximately 50 VIIRS granules mainly during the spring break-up seasons in Alaska during 2014, 2015 and 2016, and they contain information regarding supra-snow/ice floodwater (black), shadows over snow surfaces (blue) and melting snow surfaces (red). The relationship between R_{VIS} and the NDVI is shown in Fig. 2(a), Fig. 2(b) compares R_{NIR} with the NDVI, the R_{VIS} and DNDVI relationship is shown in Fig. 2(c), and Fig. 2(d) compares R_{NIR} with the DNDVI. Fig. 2 illustrates that melting snow surfaces and shadows on snow surfaces have similar values among the three variables (R_{VIS} , R_{NIR} and NDVI) and that they overlap with the scatter plot for supra-snow/ice water (Fig. 2(a) and Fig. 2(b)). However, the populations of the melting snow samples and shadow samples separate from those of the supra-snow/ice water samples with the DNDVI (Fig. 2(c) and Fig. 2(d)). Based on this, the combined use of these four variables can provide an effective approach for supra-snow/ice water detection.

3.2. Challenges

Although the spectral features of water surfaces are different from those of other land types, automatic near real-time flood detection remains challenging. The biggest challenge is the presence of cloud shadows. Cloud shadows and floodwaters are difficult to differentiate because they share similar spectral features in the Vis, NIR, SWIR, and thermal infrared channels. Geometry-based algorithms help to remove cloud shadows but are still limited due to the uncertainties regarding the cloud mask, cloud height, and cloud optical thickness.

The second challenge is the presence of terrain shadows. Like cloud shadows, terrain shadows share similar spectral characteristics to water and therefore cannot be spectrally distinguished from floodwater (Ticehurst et al., 2014). Unlike cloud shadows, which tend to change between overpass times, terrain shadows can remain for a long time. In some cases, a terrain shadow may persist for an entire winter season because of high solar zenith angles (especially at high latitudes). Cloud shadows and terrain shadows limit the autonomous flood detection in near real-time using optical satellite imagery. In addition to shadows, some dark land surfaces can exhibit similar spectral features to floodwater. For example, burn scar areas covered with a thin cover of snow can be confused with floodwater.

Other floodwater detection challenges are related to the natural environment and the physical properties of floodwater. Because a flood is an overflow of water that submerges or “drowns” land, floodwaters are impacted by the underlying conditions. Floods occur over vegetation or bare soil in the mid-latitudes, while floods occur more often over snow/ice surfaces at high latitudes and during mid-latitude winters. A mixed situation may be further complicated by the moderate spatial resolution (375 m) of SNPP/VIIRS imagery. Minor to moderate floods, which occur most frequently in the USA, may elude detection because of their weak water signal in comparison to the surrounding land signal. Some floodwaters may be masked by vegetation cover or urban development, which weaken the water signals measured by satellite imagers. Under some conditions, water surfaces are contaminated by sun glint and show substantially different spectral features in the Vis, NIR and SWIR channels relative to glint-free water surfaces.

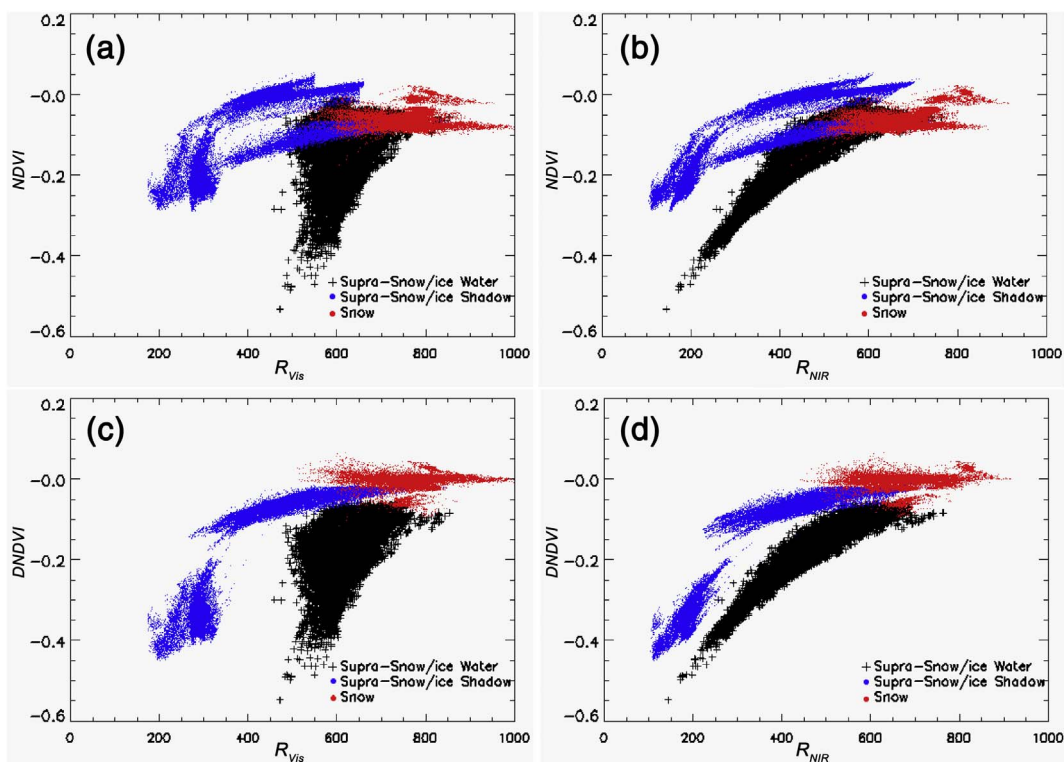


Fig. 2. Scatter plots of supra-snow/ice water (black), supra-snow/ice shadow (blue) and melting snow (red) surface in VIIRS imagery: (a) R_{Vis} and NDVI; (b) R_{NIR} and NDVI; (c) R_{Vis} and DNDVI; (d) R_{NIR} and DNDVI. (For interpretation of the references to color in this figure legend, the reader is referred to the web version of this article.)

3.3. Algorithm development

To conquer the above challenges, the algorithm development in VNG Flood V1.0 includes a series of steps ranging from water detection, cloud shadow removal, terrain shadow removal, minor flood detection, and water fraction retrieval to floodwater determination. The details of these primary algorithms in VNG Flood V1.0 are presented in the following sections from Section 3.3.1 to Section 3.3.6, and the specific algorithm flow is shown in Section 3.4.

3.3.1. Water detection

Based on the underlying conditions, floods can be divided into two types: supra-vegetation/bare soil floods (hereafter referred to as a supra-veg/bare soil flood) are the most common, and supra-snow/ice floods are generally limited to rivers flowing from low latitudes to high latitudes during spring snowmelt/break-up periods. These two flood types show different spectral features, and therefore, water detection is divided into two types: supra-veg/bare soil water detection and supra-snow/ice water detection.

In SNPP/VIIRS imagery, pixels are first classified into three types: cloud cover, snow/ice cover and land/water. Cloud cover is masked using the SNPP/VIIRS 750-m cloud mask intermediate product (IICMO). Snow/ice cover is flagged with the 375-m snow cover product or by running a snow detection module (Tsugawa and James, 2011) and is then subjected to supra-snow/ice water detection tests. The remaining pixels are classified as clear-sky land or water, which are subjected to supra-veg/bare soil water detection tests with a decision-tree approach using the following variables: R_{Vis} , R_{NIR} , R_{SWIR} , NDVI, NDSI and NDWI (Sun et al., 2012; Li and Sun, 2013). The decision trees are pre-trained based on different land cover types under different solar zenith angles by collecting approximately 600,000 samples from > 500 VIIRS granules covering North America, Africa, Europe, Asia and Australia. These pre-trained decision trees are used to separate supra-veg/bare soil water pixels from clear-sky land pixels.

Supra-snow/ice water detection constitutes an additional step

because most supra-snow/ice water locations are counted as covered by snow/ice using snow/ice detection algorithms prior to water detection. A threshold segmentation method is used with the variables R_{Vis} , R_{NIR} , NDVI and DNDVI. Based on the analysis of approximately 100 VIIRS granules, the reflectance of supra-snow/ice floodwater varies from 40% to 80% in the visible channel and from 15% to 80% in the near-infrared channel, and the NDVI ranges from -0.6 to -0.04. In comparison, the reflectance of shadows over snow/ice surfaces ranges from 15% to 65% in both the visible and near-infrared channels, and the NDVI ranges from -0.3 to 0.05. Melting snow surfaces have a reflectance that ranges from 50% to 100% in the visible and near-infrared channels while the NDVI ranges from -0.1 to 0.05. For a snow/ice pixel, if it meets the conditions in Eq. (4), it is directly classified as a supra-snow/ice water pixel without any further processing. If a snow/ice pixel meets the conditions in Eq. (5), it is then classified as a possible supra-snow/ice water pixel and is tested further against the DNDVI parameter.

$$\begin{cases} R_{\text{Vis}} \geq 45\% \\ \text{NDVI} \leq -0.2 \end{cases} \quad (4)$$

$$\begin{cases} R_{\text{Vis}} \geq 40\% \\ -0.2 < \text{NDVI} \leq -0.04 \end{cases} \quad (5)$$

The calculation of the DNDVI is a dynamic process within a moving 50×50 window (Liang et al., 2012; Johansson and Brown, 2013). For a possible supra-snow/ice water pixel, the maximum reflectance in the visible channel ($R_{\text{Vis},\max}$) of all the snow/ice pixels (based on the snow/ice cover mask) in the neighboring 50×50 window is calculated. If they meet the conditions in Eq. (6), the snow/ice pixels are collected and used to calculate the average NDVI of the background snow/ice surface ($\overline{\text{NDVI}}$). The DNDVI is calculated by subtracting $\overline{\text{NDVI}}$ from the NDVI of a possible supra-snow/ice water pixel.

$$\begin{cases} R_{\text{Vis},\max} - 10\% \leq R_{\text{Vis}} \leq R_{\text{Vis},\max} \\ R_{\text{Vis}} \geq 55\% \\ \text{NDVI} \geq -0.05 \end{cases} \quad (6)$$

The DNDVI is more effective in differentiating supra-snow/ice water from shadows over snow surfaces and melting snow surfaces. Based on a sample analysis from approximately 100 VIIRS granules, most shadows over snow surfaces with DNDVI values below -0.05 have a reflectance of $< 45\%$ in the visible channel, and those with a reflectance that is larger than 45% in the visible channel mostly exhibit a DNDVI value above -0.05 . Melting snow surfaces generally exhibit DNDVI values above -0.05 . In comparison, supra-snow/ice water demonstrates DNDVI values below -0.07 , which shows a strong relationship with the reflectance in the near-infrared channel. Therefore, if a pixel meets the condition in Eq. (7), then it is removed from the possible supra-snow/ice water pixels. This process removes most melting snow and some of the shadows that are cast upon snow surfaces from supra-snow/ice water pixels.

$$\text{DNDVI} > -0.06 \quad (7)$$

The above processes separate most of the water pixels from land and snow/ice cover pixels. However, cloud shadows and terrain shadows still need to be removed, or else they will be counted as water.

3.3.2. Cloud shadow removal

Because cloud shadows are not spectrally different from floodwater, a geometry-based method can be used to remove cloud shadows from water maps (Khlopenkov and Trishchenko, 2007; Hutchison et al., 2009; Li et al., 2013b). In this method, a spherical geometry model is established between cloud shadows and clouds and is then iteratively applied to construct a one-to-one relationship based on the assumption that one cloud pixel casts, at most, one cloud shadow pixel. If the position of a cloud pixel B ($\text{lon}_B, \text{lat}_B$) in the VIIRS imagery is known, the position of that cloud pixel P ($\text{lon}_P, \text{lat}_P$) can be located by calculating an arc using the sensor azimuth angle φ_B .

$$\text{lat}_P = \sin^{-1} \left[\sin(\text{lat}_B) \times \cos \frac{\widehat{PB}}{R} + \cos(\text{lat}_B) \times \sin \left(\frac{\widehat{PB}}{R} \right) \times \cos \varphi_B \right] \quad (8)$$

$$\text{lon}_P = \text{lon}_B + \tan^{-1} \left[\frac{\sin \varphi_B \times \sin \frac{\widehat{PB}}{R} \times \cos(\text{lat}_B)}{\cos \frac{\widehat{PB}}{R} - \sin(\text{lat}_B) \times \sin(\text{lat}_P)} \right] \quad (9)$$

The Earth's radius is R, and the arc \widehat{PB} is the parallax distance between the real cloud position P and the cloud position in the satellite imagery B.

Given the cloud position P ($\text{lon}_P, \text{lat}_P$), the cloud shadow position A ($\text{lon}_A, \text{lat}_A$) in the VIIRS imagery can be calculated using the solar azimuth angle φ_P by considering the shadow length \widehat{PA} .

$$\text{lat}_A = \sin^{-1} \left[\sin(\text{lat}_P) \times \cos \frac{\widehat{PA}}{R} + \cos(\text{lat}_P) \times \sin \left(\frac{\widehat{PA}}{R} \right) \times \cos \varphi_P \right] \quad (10)$$

$$\text{lon}_A = \text{lon}_P + \tan^{-1} \left[\frac{\sin \varphi_P \times \sin \frac{\widehat{PA}}{R} \times \cos(\text{lat}_P)}{\cos \frac{\widehat{PA}}{R} - \sin(\text{lat}_P) \times \sin(\text{lat}_A)} \right] \quad (11)$$

In Eqs. (8) through (11), \widehat{PA} and \widehat{PB} can be calculated as arcs along a circle with a radius R using a shadow angle α and a parallax angle β . The shadow angle α and parallax angle β are derived using Eq. (12):

$$\delta = \cos^{-1} \left[\frac{(R+h)^2 - (\sqrt{R \times R \times \cos^2 \theta + h \times (h+2R)} - R \times \cos \theta)^2 + R^2}{2.0 \times R \times (R+h)} \right] \quad (12)$$

where δ represents the shadow angle α or parallax angle β , R is the Earth's radius, h is the cloud height, and θ is the zenith angle.

In contrast, if the shadow position A ($\text{lon}_A, \text{lat}_A$) is known, then Eqs. (8) through (12) can also be used to predict the cloud position B ($\text{lon}_B, \text{lat}_B$) on the spherical surface in the VIIRS imagery.

Based on the geometric model over a spherical surface, an iteration method is further applied to the cloud height, which is the only

unknown variable in Eqs. (8) through (12), to construct a one-to-one relationship between the cloud and cloud shadow using a group of adjacent cloud and cloud shadow pixels. Here, the cloud height is coarsely estimated using cloud top temperatures and nearby clear-sky land surface temperatures under average atmospheric temperature profiles. Tests conducted on a large amount of VIIRS imagery and more than three years' worth of demonstrations have proven that this method removes $> 90\%$ of the cloud shadows from VIIRS flood maps.

3.3.3. Terrain shadow removal

Similar to cloud shadows, most terrain shadows are classified as floodwater during water detection. To remove terrain shadows, an object-based method is applied using 375-m DEM data resampled from SRTM-2 and ASTER data based on the surface roughness (Li et al., 2015). Because terrain shadows generally appear in mountainous topography, the surface roughness is usually much larger than floodwater, which mainly accumulates in low-lying areas (where the surface roughness is lower) (Shepard et al., 2001; Thompson et al., 2011). The method is object-based, and thus, a surface roughness analysis is performed on a group of adjacent pixels instead of on single pixels. Water pixels are clustered into a group and viewed as one object for calculating the surface roughness parameters. A floodwater object is determined as a terrain shadow if it meets the conditions in Eq. (13):

$$\gamma \geq 60, \text{ or}, \begin{cases} \gamma_{\text{th}} \leq \gamma < 60 \\ D_{\text{ave}} \geq D_{\text{ave,th}}, \text{ or}, \begin{cases} \gamma_{\text{th}} + 5 \leq \gamma < 60 \\ D_{\text{ave}} \geq D_{\text{ave,th}} + 20 \end{cases} \\ |D_n| \geq 3 \\ N_w \leq 1 \end{cases} \quad (13)$$

where γ is the root-mean-square height, D_{ave} is the internal height difference between the average heights of the higher surface and the lower surface, D_n is the external height difference between the average heights of neighboring non-shaded or non-flooding land pixels and the average heights of terrain shadow or floodwater pixels, N_w is total number of normal water pixels, P_w is the percentage of normal water pixels, and γ_{th} and $D_{\text{ave,th}}$ are the empirical thresholds of γ and D_{ave} , which are related to the total number of water/shadow pixels and the total length in both the horizontal and vertical directions in an object.

This method has been applied to the removal of terrain shadows from VIIRS flood maps. A validation analysis has shown that this method removes $> 95\%$ of the terrain shadows from VIIRS flood maps, and it also helps to remove other false water detection results, such as some residual cloud shadows, dark lava land and burn scars (Li et al., 2015).

3.3.4. Minor flood detection

At a 375-m spatial resolution, water signals from many minor floods are too weak to be detected in VIIRS imagery, especially when floodwaters are veiled by vegetation cover or urban development. The majority of floods in the USA are minor floods, but they still attract the attention of river forecasters. Change detection is used as the main approach to detect minor floods around water pixels, as confirmed in the steps described from Section 3.3.1 to Section 3.3.3, and existing rivers, lakes, and reservoirs in ancillary water reference maps. The method determines a minor water pixel either by comparing water signals from before and after flooding or by comparing water signals with surrounding confirmed clear-sky land pixels that have similar land cover types to the minor water pixel.

For automatic near real-time flood detection, less dependence is placed on historic data in favor of an additional comparison with surrounding clear-sky land pixels. For a confirmed water pixel, the average reflectance in the near-infrared and shortwave infrared channels are calculated in neighboring 50×50 windows for vegetation ($\overline{R}_{\text{NIR,V}}$, $\overline{R}_{\text{SWIR,V}}$) and bare land ($\overline{R}_{\text{NIR,B}}$, $\overline{R}_{\text{SWIR,B}}$), respectively. Land pixels around the confirmed water pixel, which cannot be 30 m higher in elevation than the confirmed water pixel, are then used within a

reflectance comparison relative to the average reflectance. If it meets the conditions in Eq. (14), a vegetation pixel is determined as a minor water pixel; meanwhile, if a bare land pixel meets the conditions in Eq. (15), then it is determined as a minor water pixel.

$$\begin{cases} R_{NIR} \leq 26\% \\ R_{SWIR} \leq 15\% \\ \overline{R_{NIR,V}} - R_{NIR} \geq 8\% \\ \overline{R_{SWIR,V}} - R_{SWIR} \geq 4\% \\ \text{NDSI} > -0.12 \end{cases} \quad (14)$$

$$\begin{cases} R_{NIR} \leq 25\% \\ R_{SWIR} \leq 17\% \\ \overline{R_{NIR,B}} - R_{NIR} \geq 7\% \\ \overline{R_{SWIR,B}} - R_{SWIR} \geq 8\% \\ \text{NDSI} > -0.15 \end{cases} \quad (15)$$

3.3.5. Water fraction retrieval

Due to the moderate spatial resolution of the VIIRS data, most detected flood pixels are a mixture of water and other land types, such as vegetation, bare soils or snow/ice. The water fraction, which is defined as the percentage of the water surface in a satellite pixel, represents the flood status more accurately than a simple water/no water mask classification (Sheng and Gong, 2001). For flood detection using VNG Flood V1.0, only supra-veg/bare soil floodwaters are retrieved for the water fractions. A dynamic nearest neighbor search (DNNS) method based on a linear combination model is applied by considering the varying sub-pixel land portion in a land-water mixed pixel and counting the adjacent land pixels with similar mixture ratios to estimate the reflectance of the land for the retrieval (Li et al., 2012). The linear combination model for the water fraction retrieval is expressed in Eq. (16):

$$f_w = \frac{R_{land} - R_{mix}}{R_{land} - R_{water}} \quad (16)$$

where R_{mix} is the reflectance of a land-water mixed pixel, which is directly obtained from the VIIRS imagery, R_{land} is the reflectance of pure land that meets condition (16), and R_{water} is the reflectance of a pure water surface, which is calculated as the average reflectance of adjacent pure water pixels. Because R_{water} is small in the Vis and NIR channels and is close to 0 in the SWIR channel, the accuracy of f_w largely depends on R_{land} . By combining the Vis, NIR and SWIR channels, R_{land} is calculated as the average reflectance of pure land pixels located nearby that meet conditions in Eq. (17), after which it is then applied in Eq. (16) to calculate f_w . An evaluation analysis shows that the method performs more robustly than the traditional histogram method for the retrieval of supra-veg/bare land water fractions, especially when the sub-pixel land portion contains complex land types (Li et al., 2012).

$$\begin{aligned} \frac{R_{Vis,mix}}{R_{SWIR,mix}} - \frac{R_{Vis,water}}{R_{SWIR,mix}} &< \frac{R_{Vis,land}}{R_{SWIR,land}} < \frac{R_{Vis,mix}}{R_{SWIR,mix}} \\ \frac{R_{NIR,mix}}{R_{SWIR,mix}} - \frac{R_{NIR,water}}{R_{SWIR,mix}} &< \frac{R_{NIR,land}}{R_{SWIR,land}} < \frac{R_{NIR,mix}}{R_{SWIR,mix}} \end{aligned} \quad (17)$$

3.3.6. Flood determination

The retrieved supra-veg/bare soil water fractions are compared against the water reference map, which is a combination of the MODIS 250-m global water mask and the water layer in the 30-m National Land Cover Dataset (for the USA). The MODIS 250-m global water mask is resampled to a 375-m water/no water mask using a nearest neighbor interpolation method to spatially match it with the VIIRS imagery, while the 30-m National Land Cover Dataset is resampled to a 375-m water mask by calculating the water fractions in 375-m grids. In the USA, where a water reference map is equipped with water fraction information, if the water fraction of a pixel in the water reference map is $< 1\%$ (which makes it a land pixel), then the floodwater is

determined directly and represented with the retrieved fraction. If the water fraction of a pixel is $> 1\%$ in the water reference map, then the floodwater is only determined if the retrieved water fraction is at least 40% larger than that in the water reference map. In regions outside of the USA where water reference maps are made using the MODIS water/no water mask, a water pixel is directly determined as floodwater and assigned with its retrieved water fraction if it is a non-water (land) pixel in the water reference map.

To differentiate ice from water using supra-veg/bare soil in VIIRS flood maps, supra-snow/ice water is classified as one type and represented in a simple water/no water mask without any fraction retrieval data. Supra-snow/ice floodwater can also be determined by comparing it against the water reference map; however, supra-snow/ice water within river channels and lakes is retained to reflect information on the river/lake ice status.

Therefore, in VIIRS flood maps, supra-veg/bare soil floodwater pixels are represented with fractions ranging from 1% to 100%, which provides end-users with more detail on the extent of flooding, while supra-snow/ice water is represented as an independent water/no water type without fraction retrieval and flood determination information.

3.4. Algorithm process

The algorithm steps detailed in Section 3.3 are integrated into VNG Flood V1.0 for near real-time flood detection. VIIRS SDR data and EDR products undergo a re-projection process, the flood detection algorithm is run, and the imagery is finally produced. Fig. 3 presents the specific algorithm processing flow of the software. The flood detection process starts by applying the VIIRS cloud mask to remove cloud cover. Next, snow/ice cover is flagged using VIIRS snow/ice detection. Based on the snow/ice cover, the threshold segmentation method shown in Section 3.3.1 is applied to determine supra-snow/ice water pixels. The rest of the clear-sky pixels are classified with a decision-tree approach as described in Section 3.3.1 for vegetation, bare soil and supra-veg/bare soil water. All of the detected water pixels (including the supra-snow/ice water pixels and supra-veg/bare soil water pixels) are subjected to the geometry-based cloud shadow removal algorithm shown in Section 3.3.2 (to remove cloud shadow pixels) and the object-based terrain shadow removal algorithm presented in Section 3.3.3 (to remove terrain shadows). Most shadow pixels are identified by one of these shadow detection processes, and those that remain are categorized as water pixels. Based on the supra-veg/bare soil water pixels and water bodies defined in the water reference map, a change detection approach described in Section 3.3.4 is used to identify water pixels in minor flood detection that were not detected by the decision-tree approach. A DNNS method presented in Section 3.3.5 is then utilized to retrieve the supra-veg/bare soil water fractions. The retrieved supra-veg/bare soil water fractions are further compared against the water reference map to determine the floodwater using the method shown in Section 3.3.6. Ultimately, there are eight pixel types in the final VIIRS flood map: cloud, snow cover, river/lake ice cover, shadows (including cloud shadows and terrain shadows), clear-sky land (including vegetation and bare soil), normal open water, supra-snow/ice water, and supra-veg/bare soil flooding water fractions.

4. Results

4.1. Applications

During a demonstration project operated by the JPSS PGRR Program since 2014, the developed VNG Flood V1.0 has been running routinely for five river forecast centers in the USA at two locations that process VIIRS direct broadcast data in near real-time: the Space Science and Engineering Center at the University of Wisconsin-Madison (SSEC/UW-Madison) and the Geographic Information Network of Alaska at the University of Alaska-Fairbanks (GINA/UAF). The flood maps are

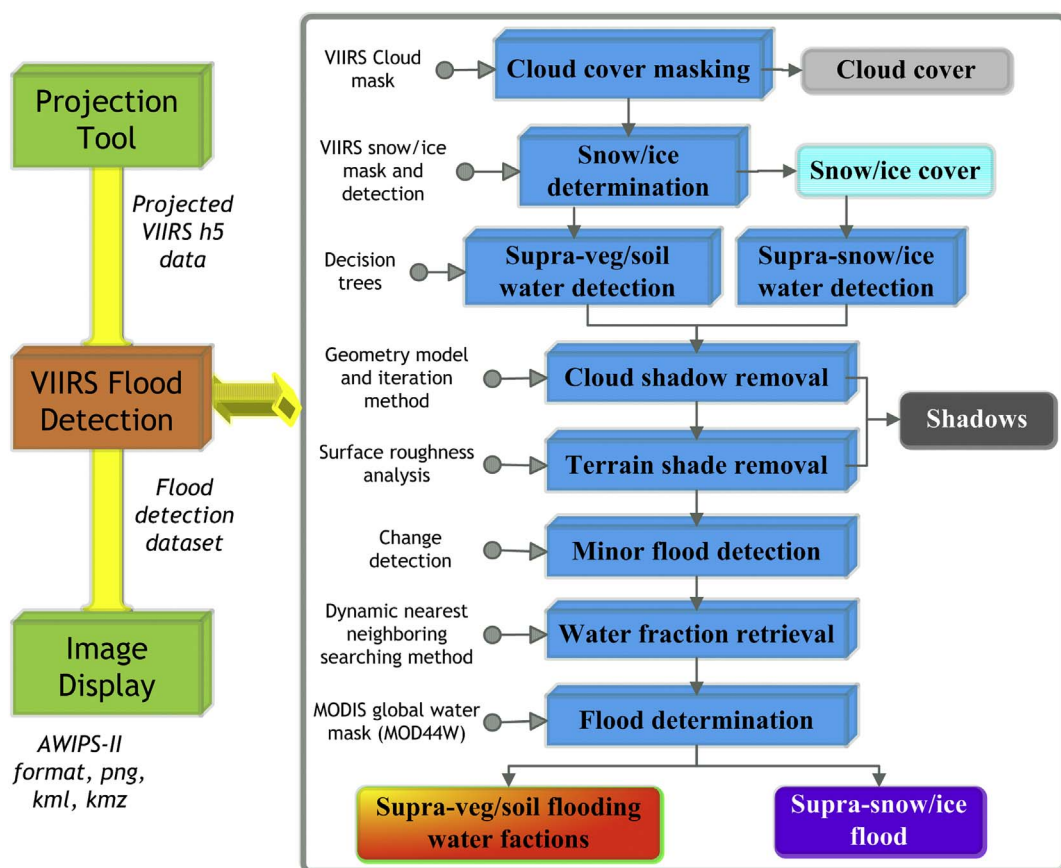


Fig. 3. Algorithm flow chart of VNG Flood V1.0.

distributed via the Unidata Local Data Manager (LDM) and are reviewed by river forecasters in AWIPS-II. Additionally, these near real-time flood maps are available in the SSEC Real Earth application for Internet users to browse via a web link: <http://realearth.ssec.wisc.edu/?products=RIVER-FLDall-US>. During the demonstration, VIIRS near real-time flood products are evaluated by river forecasters using aerial photos and river gauge observations. The flood products have been increasingly used as a tool to help issue operational flood forecasts. The evaluations have shown that the products perform robustly and have detected many floods accurately, including some minor floods. Positive responses have been received from river forecasters who cite the product as being a near real-time resource capable of providing useful situational awareness information for flood monitoring and forecasting.

4.1.1. Application in dynamic flood extent monitoring

The most straightforward application of the VIIRS flood products is dynamic flood extent monitoring, which makes the product an important data source for river forecasters to stay aware of flooding situations. With VIIRS near real-time flood maps, floodwaters can be identified and dynamically monitored. Compared to binary water/no-water flood products, floodwater fractions provide more details of the flood extent and intensity. Fig. 4 presents four flood maps during the December 2015 Mississippi River flood. In Fig. 4, the spatial distribution of the floodwater extent is shown throughout the Illinois River Basin, the Ohio River Basin and the Lower Mississippi River Basin clearly and continuously. These flood products were monitored through this event and provided river forecasters with valuable situational awareness information that was incorporated into the forecasting process. The wide coverage, moderate spatial resolution and frequent observations reflect the unique advantages of VIIRS imagery for near real-time flood mapping in comparison to imagery from other satellites such

as Landsat.

VNG Flood V1.0 is designed for flood mapping in any land region between 80°S and 80°N using VIIRS global imagery, and thus, its flood detection capabilities, which have frequently been applied to flood mapping during flood events in Asia, Australia, Africa and South America, have also been extended to regions outside of the USA. Fig. 5 shows two example flood maps for Australia and Peru. Fig. 5(a) is a flood map in Queensland, Australia, on 31 Mar. 2017 at 04:19 (UTC) after cyclone Debbie struck the region. Fig. 5(b) is a flood map in Peru on 23 Mar. 2017 at 18:45 (UTC). In Fig. 5, the floodwater extent is clearly demonstrated and represented with water fractions. These flood maps may help river forecasters and decision-makers to investigate flood statuses in a timely manner.

4.1.2. Application in snow-melt and ice-jam flood prediction and monitoring

Most snowmelt and ice-jam floods can be observed continuously with VIIRS near real-time flood maps because they are less affected by cloud cover than floods caused by intense rainfall. Snow/ice cover available in the flood maps presents the details of ice-jam locations and snowmelt runoff progression, and floods can be tracked as an event develops, thereby providing important information for flood forecasting and early warning. Fig. 6 shows a series of flood maps for the severe ice-jam flood near Galena, Alaska (AK) in 2013. On 26 May 2013 (Fig. 6(a)), a larger section of the Yukon River near Galena, AK, was covered with river ice, and an ice jam formed downstream of Galena. On 27 May 2013 at 20:45 (UTC), ice break-up occurred in the upper river reaches, but the ice jam remained in place near Galena, causing water to back up and flood overland. Some flooded areas were seen developing near the jammed section (Fig. 6(b)). The floodwater expanded rapidly, and two hours later, additional floodwater was detected (Fig. 6(c)). As the flooding continued to expand overland,

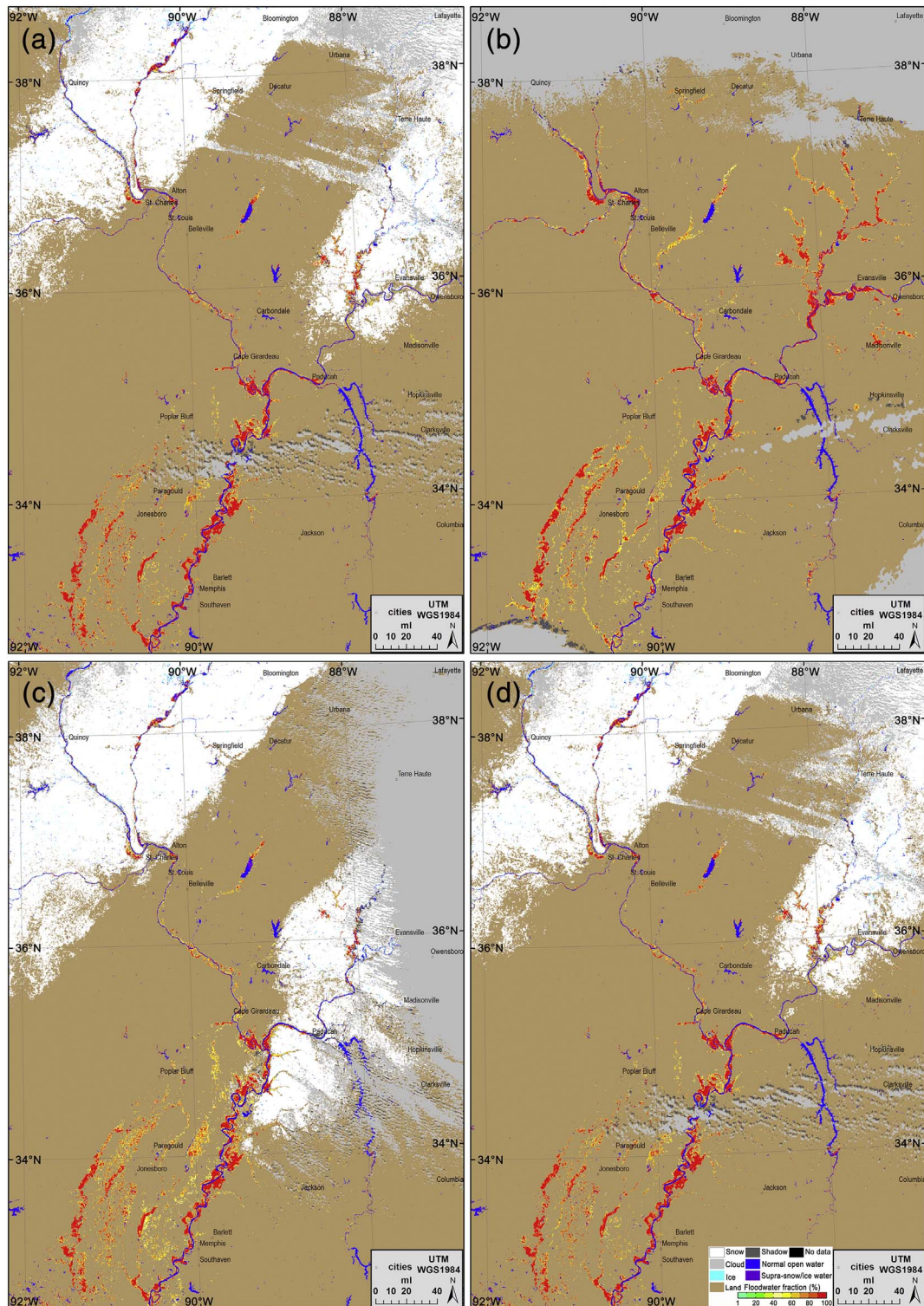


Fig. 4. SNPP/VIIRS near real-time flood detection maps in the Mississippi River Basin between 01 Jan. 2016 and 12 Jan. 2016: (a) 01 Jan. 2016 18:45 (UTC); (b) 03 Jan. 2016 19:48 (UTC); (c) 10 Jan. 2016 19:18 (UTC); (d) 12 Jan. 2016 18:40 (UTC).

additional flooded areas appeared in the SNPP/VIIRS flood maps on 28 May (Fig. 6(d)–(f)). On 29 May, the jam began to release and the pixel types changed from ice cover to overflow/mixed water and ice types (Fig. 6(g)). On 30 May, the jam disappeared and the river became open as the floodwaters started to retreat (Fig. 6(h)), and on 1 June, fewer floodwaters were detected as the flooding continued to recede (Fig. 6(i)). The continuous SNPP/VIIRS observations demonstrated the dynamic progress of this river ice-jam flooding event, and the

information provided by the flood maps were very valuable for flood prediction and monitoring.

VIIRS flood products can be applied to many other areas. For example, the flooding water fraction product is an important input of a downscaling model to derive high-resolution flood maps (Li et al., 2013a). The VNG Flood V1.0 product can also be used to discover new water bodies from impoundment projects or condition changes of seasonal lakes. Long-term VIIRS flood maps are a good data source for

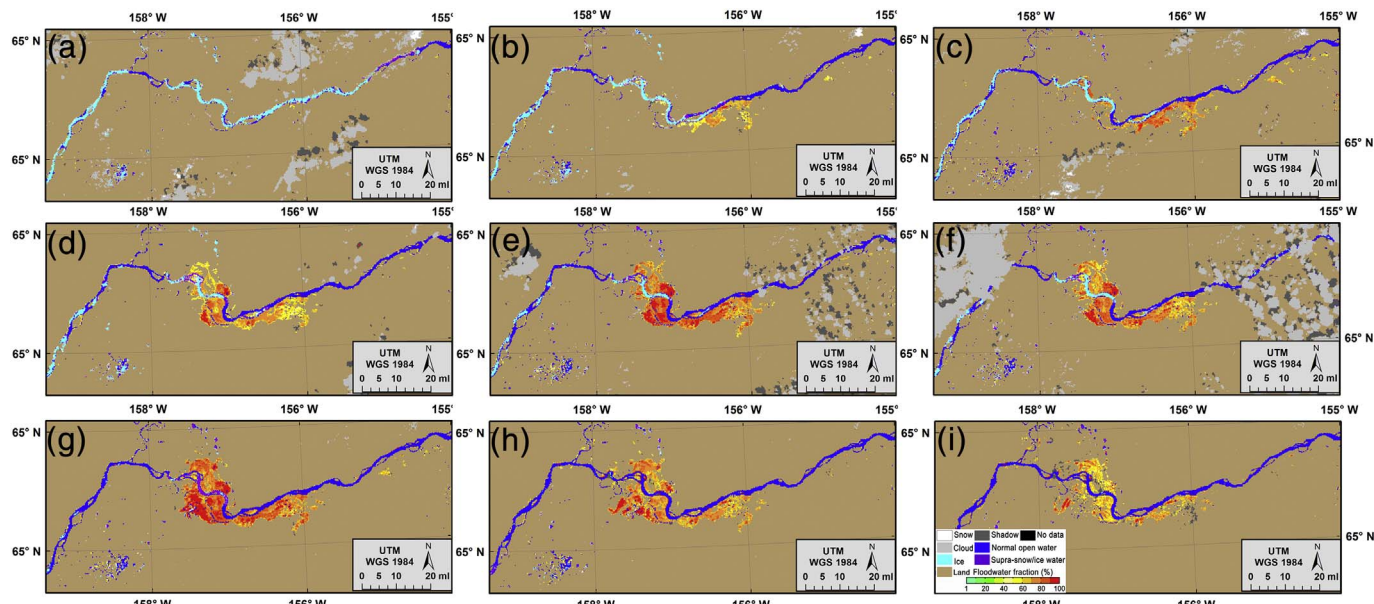


Fig. 5. SNPP/VIIRS near real-time flood detection maps in Australia and Peru: (a) VIIRS flood map in Queensland, Australia on 31 Mar. 2017 04:19 (UTC); (b) VIIRS flood map in Peru on 23 Mar. 2017 18:45 (UTC).

flood pattern analysis and wet agricultural area estimations (e.g., rice paddies). All of these applications offer proof of the high value of the near real-time flood product from SNPP/VIIRS imagery.

4.2. Evaluation

4.2.1. Visual inspection

In addition to near real-time processes, the product has also been evaluated offline with VIIRS imagery since 2013. Over 10,000 VIIRS granules have been tested and visually inspected with VIIRS false-color

composite images with VIIRS imager bands 3 (red), 2 (green) and 1 (blue). These granules cover most of the global land areas between 80°S and 80°N year-round. Visual inspection consistently shows a promising product performance. Fig. 7 depicts an example of the visual inspection validation. Fig. 7(a) is a VIIRS false-color image on 19 May 2015 at 21:35 (UTC) in northern Alaska, and the corresponding VIIRS flood detection map is shown in Fig. 7(b). In Fig. 7(a), the cyan color indicates that there was still snow cover in that area, some clouds (shown in light gray-white) and cloud shadows (darker gray). In the southeast part of the image, the topography causes some dark terrain shadows.

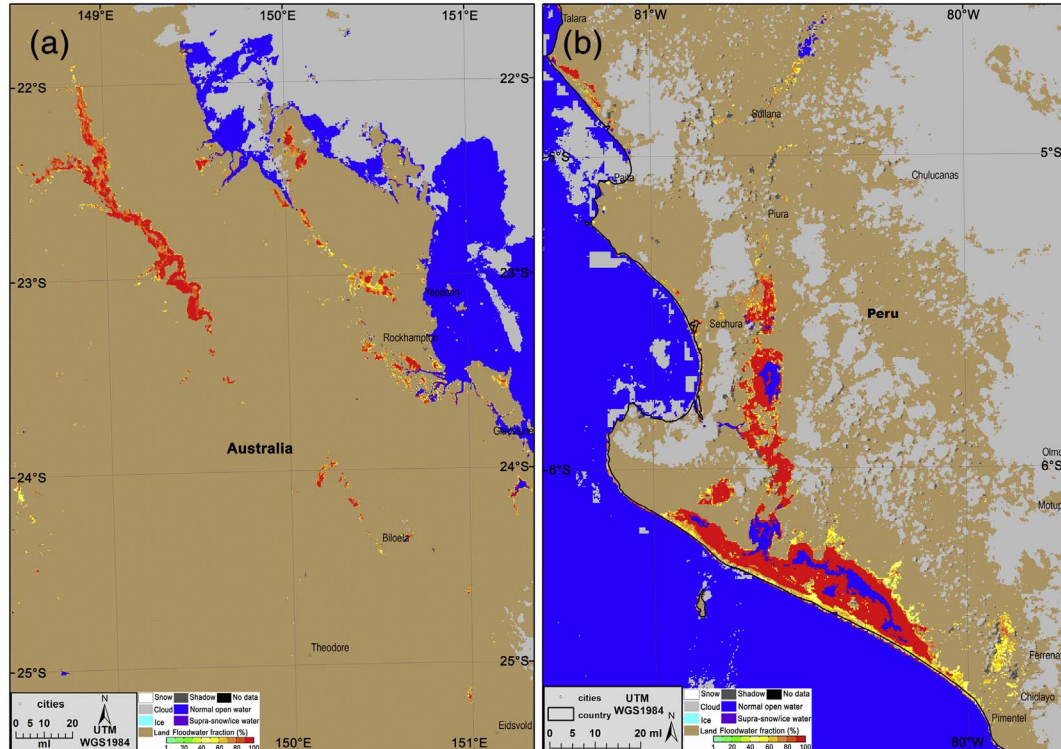


Fig. 6. SNPP/VIIRS ice-jamming flood detection maps around Galena, Alaska of USA: (a) 26 May 2013 20:45 (UTC); (b) 27 May 2013 20:27 (UTC); (c) 27 May 2013 22:04 (UTC); (d) 28 May 2013 20:10 (UTC); (e) 28 May 2013 21:46 (UTC); (f) 28 May 2013 23:29 (UTC); (g) 29 May 2013 21:29 (UTC); (h) 30 May 2013 21:11 (UTC); (i) 1 June 2013 22:13(UTC).

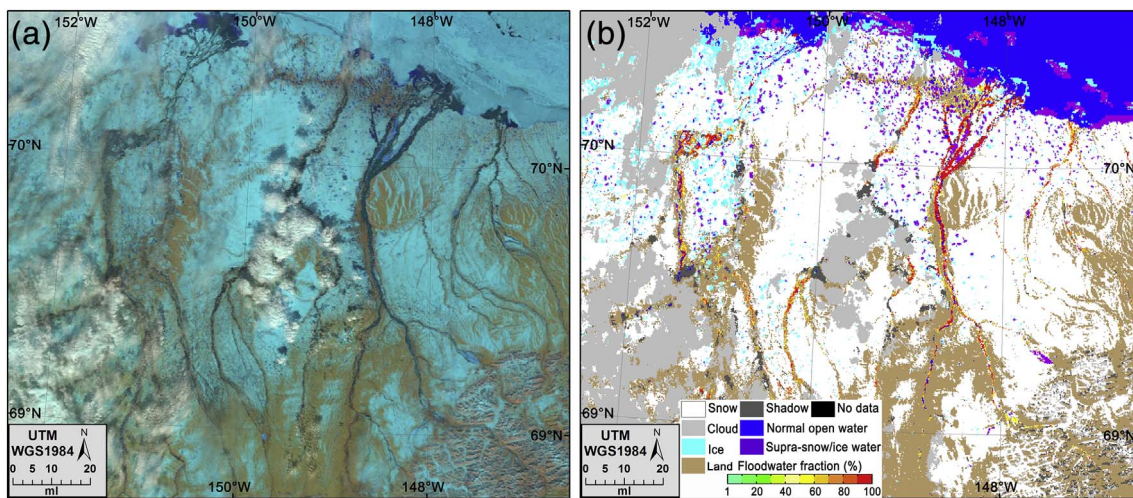


Fig. 7. (a) SNPP/VIIRS false-color composite image in north Alaska on 19 May 2015 21:35 (UTC); (b) SNPP/VIIRS flood detection map in north Alaska on 19 May 2015 21:35 (UTC).

During northern Alaska's break-up and snow-melting season, ice jams and snowmelt atop the snow/ice surfaces often cause flooding. The situation in Fig. 7(a) is a complex scene, yet Fig. 7(b) shows realistic results from an automatic near real-time flood detection product. Clouds are masked (shown in gray) and snow/ice cover is flagged (white). River/lake ice is detected (cyan), cloud shadows and terrain shadows are removed (dark gray), and supra-snow/ice water is depicted over some river channels and lakes (purple). Supra-veg/bare soil floodwaters are represented as water fractions (from light green to red), and the rest of the clear-sky land, including vegetation and bare soil, is shown in light brown. These consistent depictions indicate that the product performs well under complex weather and ground conditions.

4.2.2. Comparison with MODIS automatic flood products

MODIS experimental automatic flood products were publicly released in 2011 by NASA based on Dartmouth's flood detection algorithms, and they are available in 2-day, 3-day and 14-day composite flood maps at the following website: <http://oas.gsfc.nasa.gov/floodmap>. During some flood events, daily near real-time (1-day) flood maps are also available at this website. To remove cloud shadows and terrain shadows, a composition process is applied based on multiple-day flood maps. This process sometimes misclassifies floodwater as shadows and under-reports floodwater in the MODIS 2-day and 3-day composite flood maps. VNG Flood V1.0 removes cloud shadows and terrain shadows during each overpass and is therefore able to produce near real-time flood maps with less shadow bias. Fig. 8 presents an example showing the differences between the two flood products during the January 2017 California flood. Fig. 8(a) is MODIS false-color composite image on 11 Jan. 2017 at 19:10 (UTC) that was downloaded from the MODIS Today, website (<http://ge.ssec.wisc.edu/modis-today>), and Fig. 8(b) is a MODIS flood map using 1-day, 2-day and 3-day composite floodwater shapefiles downloaded from the following website: <http://oas.gsfc.nasa.gov/floodmap>. In Fig. 8(b), blue colors represent floodwater in the MODIS 3-day composite floodwater layer from 09 to 11 Jan. 2017, green and blue colors represent floodwater in the MODIS 2-day composite floodwater layer from 10 to 11 Jan. 2017, and red, green and blue show MODIS 1-day near real-time floodwater on 11 Jan. 2017 at 19:10 (UTC). An SNPP/VIIRS false-color composite image and the corresponding automatic flood detection map on 11 Jan. 2017 at 21:16 (UTC) produced by VNG Flood V1.0 are shown in Fig. 8(c) and (d), respectively. In the MODIS false-color image (Fig. 8(a)), the floodwaters are visible as dark blue. Most of these floodwaters are successfully identified in the MODIS 1-day floodwater layer (red, green and blue in Fig. 8(b)). However, many cloud shadows and terrain shadows are misclassified as floodwater. The composition

process results in fewer cloud shadows in the 2-day composite floodwater layer (green and blue in Fig. 8(b)), but much of the valid floodwater identified in the 1-day floodwater layer is removed. Furthermore, the 3-day composite floodwater layer (blue in Fig. 8(b)) has almost no shadows, but almost all of the floodwater is removed as well. The weather conditions changed slightly between the 19:10 (UTC) Terra-MODIS overpass and the 21:16 (UTC) SNPP-VIIRS overpass, and those cloud cover changes resulted in some different areas where the floodwater is obscured by clouds. Despite these complex conditions, which are depicted in the VIIRS false-color composite image (Fig. 8(c)), the VNG flood detection results (Fig. 8(d)) are still highly consistent with the false-color composite image. Overall, the floodwater detected in the VIIRS flood map corresponds well with the flooding that is apparent in the imagery as well as the 1-day MODIS floodwater layer. Cloud shadows and terrain shadows (dark gray in Fig. 8(d)) have been separated from the floodwater in the VNG flood product more effectively than in the MODIS flood product.

Two days later, on 13 Jan. 2017, clear skies offered a good view of the flooding in California. Because there were clear skies on 11 Jan. and 13 Jan. 2017, but there were partially cloudy skies on 12 Jan. 2017, the MODIS 2-day composite floodwater layer from 12 to 13 Jan. (green and blue in Fig. 9(a)) show similar floodwaters as those in the 3-day (from 11 Jan. to 13 Jan.) composite floodwater layer (blue in Fig. 9(a)). However, around the mountains (especially in the southern region), some terrain shadows erroneously appear as floodwaters in the MODIS 2-day composite floodwater layer. With the further application of the composition process, most of the terrain shadows in the 2-day composite floodwater layer disappeared in the MODIS 3-day composite floodwater layer. Compared with the MODIS flood products, a similar floodwater distribution was depicted, but the terrain shadows along the mountains were accurately identified in the VNG flood map (Fig. 9(b)).

To further analyze the differences between the two flood products, the MODIS 250-m floodwater datasets in California on 11 Jan. and 13 Jan. 2017 are resampled to a 375-m spatial resolution for a comparison with the VIIRS flood datasets pixel-by-pixel. The floodwaters are interactively extracted, or manually extracted and corrected via visual inspection on multiple-channel satellite images, from the 11 Jan. MODIS data and the 13 Jan. VIIRS data and are further used as reference maps for comparison. Fig. 10(a) shows the interactively extracted floodwater from MODIS data on 11 Jan. 2017 19:10 (UTC), and VIIRS interactively extracted results on 13 Jan. 2017 20:38 (UTC) are presented in Fig. 10(b). The total number of floodwater pixels (N_{total}) is calculated from the MODIS near real-time (1-day), 2-day composite and 3-day composite floodwater datasets and the VIIRS near real-time floodwater datasets. If a floodwater pixel is correspondingly shown in

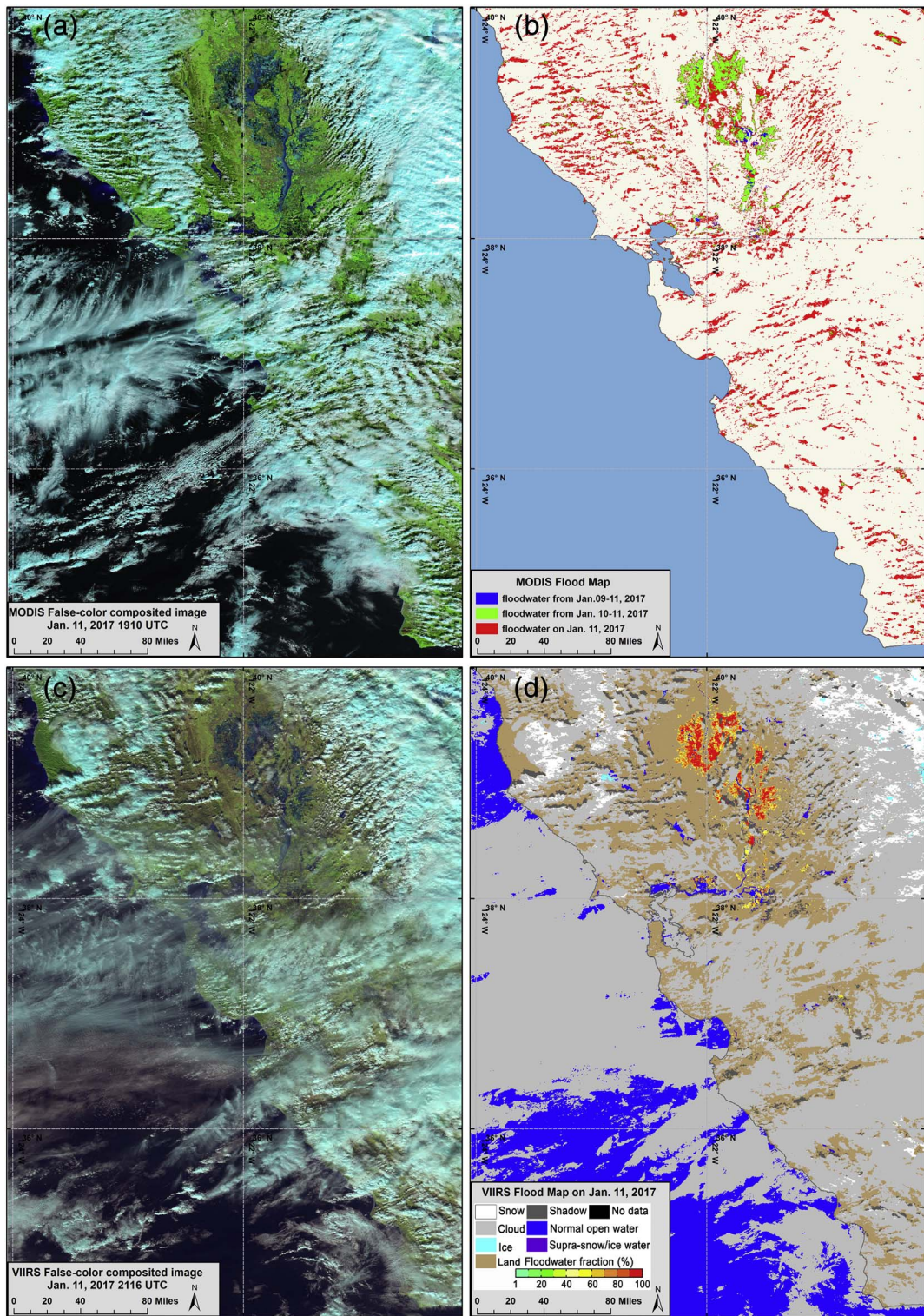


Fig. 8. (a) MODIS false-color composite image on 11 Jan. 2017 at 19:10 (UTC); (b) MODIS near real-time, 2-day and 3-day composited flood map in California, USA on 11 Jan. 2017; (c) SNPP/VIIRS false-color composite image on 11 Jan. 2017 at 21:16 (UTC); (d) SNPP/VIIRS near real-time flood map produced by VNG Flood V1.0 on 11 Jan. 2017 at 21:16 (UTC).

the reference map, then that pixel is considered a true floodwater pixel, and thus, N_t represents the total number of true floodwater pixels. If a flood pixel in the reference map is shown as clear-sky land in either the MODIS or VIIRS flood map, then that pixel is considered an undetected floodwater pixel, and thus, the total number of undetected floodwater pixels is N_u . The false detection ratio P_f , detection accuracy rate P_d , and omission ratio (undetected ratio) P_O are calculated in Eqs. (18), (19) and (20), respectively, as follows:

$$P_f = \frac{N_{total} - N_t}{N_{total}} \times 100\% \quad (18)$$

$$P_d = \frac{N_t}{N_{total} + N_u} \times 100\% \quad (19)$$

$$P_O = \frac{N_u}{N_t + N_u} \times 100\% \quad (20)$$

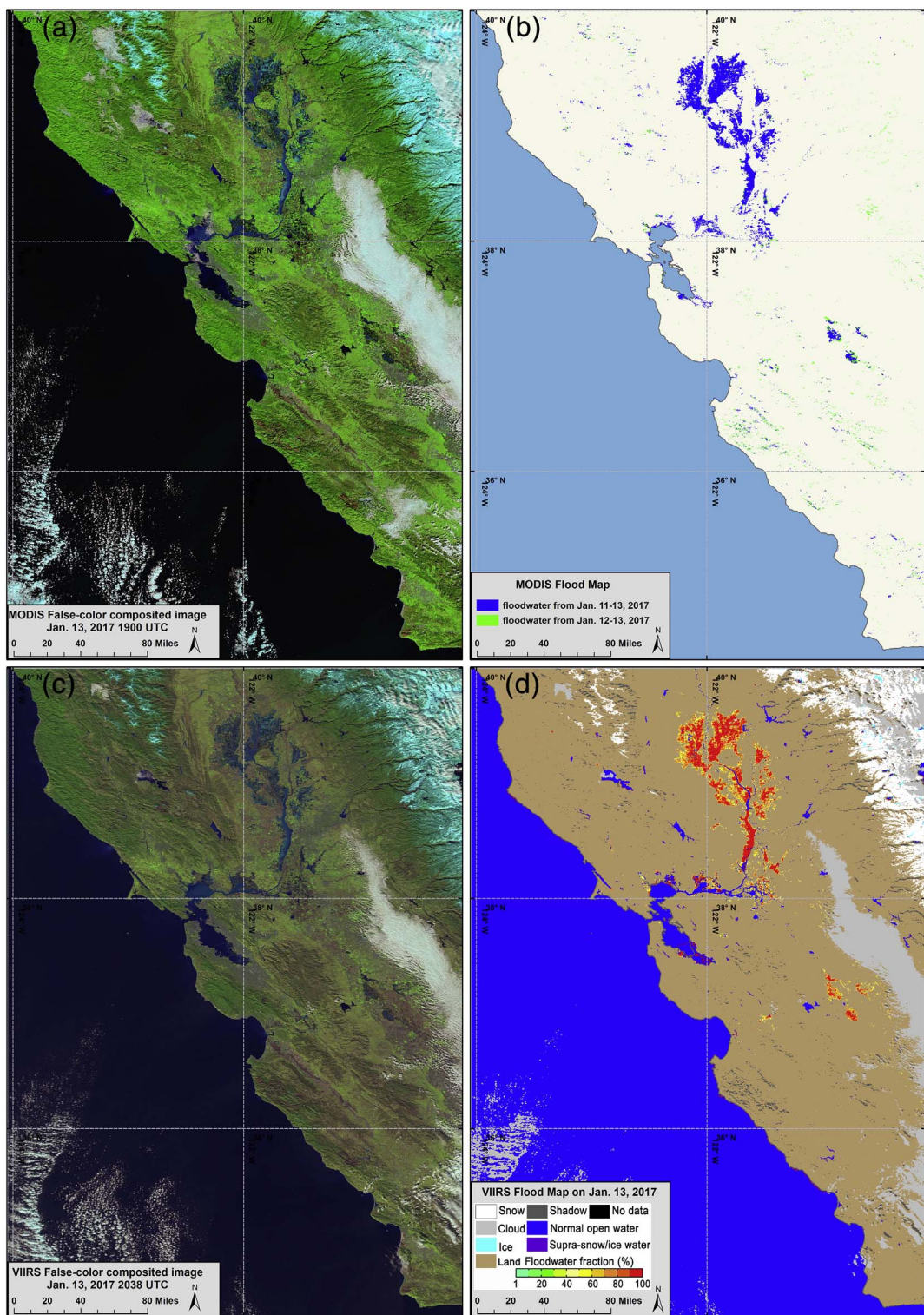


Fig. 9. (a) MODIS false-color composite image on 13 Jan. 2017 at 19:00 (UTC); (b) MODIS 2-day and 3-day compositing flood map in California, USA on 13 Jan. 2017; (c) SNPP/VIIRS false-color composite image on 13 Jan. 2017 at 20:38 (UTC); (d) SNPP/VIIRS flood map produced by VNG Flood V1.0 on 13 Jan. at 20:38 (UTC).

Table 1 lists the results for the Jan. 2017 California flood event from the MODIS and VIIRS data. From **Table 1**, the MODIS flood map on 11 Jan. 2017, detected 135,797 flood pixels altogether, but only 28,602 pixels were true floodwater pixels, and 8286 flood pixels remained undetected. The false detection ratio was approximately 78.94%. With a 2-day composition process, only 22,384 flood pixels were detected, of which 16,732 pixels were true flood pixels. Compared to the MODIS near real-time flood detection results, the false detection ratio for the 2-

day composition process decreased to 25.25%. However, the number of undetected flood pixels N_u reached 20,156, resulting in a 54.64% omission ratio. After the 3-day composition process, only 1435 flood pixels were detected, of which 1129 pixels were true flood pixels. The false detection ratio decreased to 21.32%, but N_u increased to 35,759, and the omission ratio reached 96.94%, which indicates that most of the floodwater pixels in the MODIS 3-day flood map were filtered out by the 3-day composition process. With more clear-sky weather

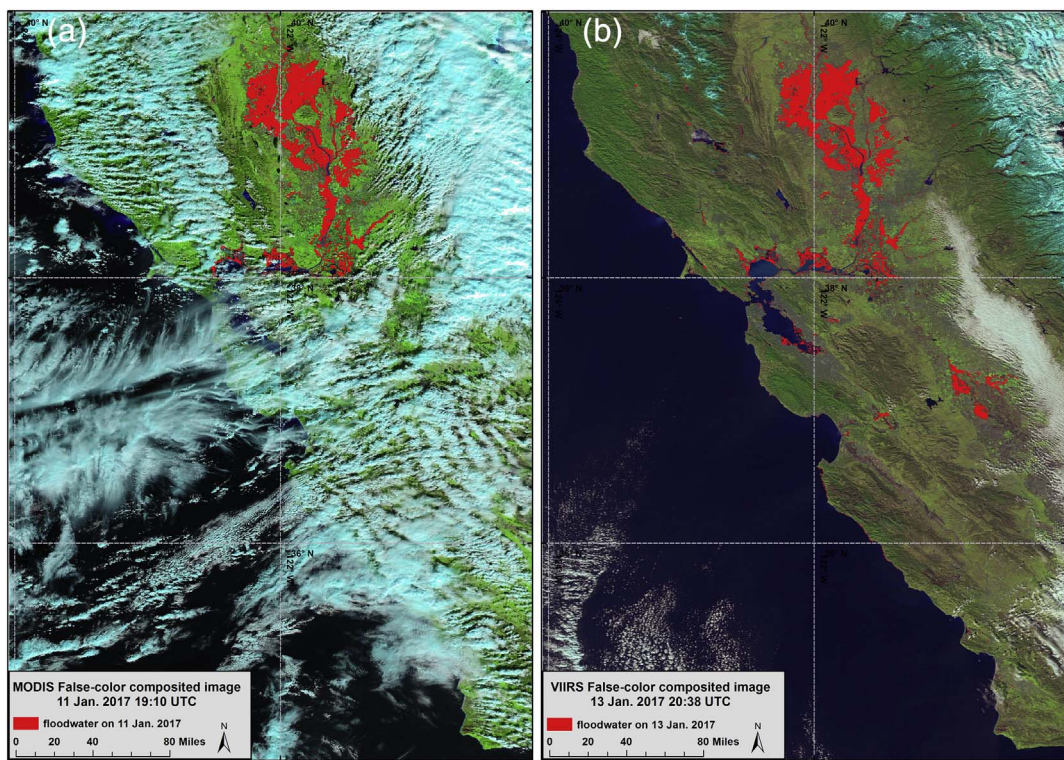


Fig. 10. (a) MODIS interactively extracted floodwater on 11 Jan. 2017 at 19:10 (UTC); (b) VIIRS interactively extracted floodwater on 13 Jan. 2017 at 20:38 (UTC).

conditions on 13 Jan., MODIS showed better detection results. In the MODIS 2-day composite flood map, 34,387 flood pixels were detected altogether, of which 24,362 pixels were true flood pixels. Approximately 16,982 flood pixels remained undetected. The false detection ratio and omission ratio were 29.15% and 41.07%, respectively. With a 3-day composition process, the MODIS results showed 29,572 detected flood pixels, 24,298 true flood pixels and 17,571 undetected flood pixels. The false detection ratio and omission ratio were 17.83% and 41.97%, respectively. In comparison, the VIIRS near real-time flood map on 11 Jan. 2017 detected 25,258 flood pixels, of which 23,773 pixels were true flood pixels. Approximately 4257 flood pixels were undetected. The false detection ratio was only 5.88%, and the omission ratio was approximately 15.19%. With much better weather conditions on 13 Jan., the VIIRS flood map detected 42,499 flood pixels altogether on that day, of which 41,290 were true flood pixels. Only 23 flood pixels were undetected. The false detection ratio was 2.84%, and the omission ratio was only 0.06%. The difference of omission ratios between MODIS and VIIRS especially on Jan. 13 with clear-sky weather conditions might reflect the impact of minor flood detection on the product performance. With minor flood detection, pixels with small water fractions (water fraction from 25% to 50%), most of which were detected as dry land in MODIS flood maps, were detected as water in VIIRS flood maps, resulting in larger omission ratios of MODIS flood maps but smaller ones of VIIRS flood maps. The results of the

comparison indicate more steady detection for VNG Flood V1.0 compared to that of the MODIS flood maps for both complex and clear-sky weather conditions. The improved performance, especially with regard to the removal of cloud shadows and terrain shadows, guarantees the near real-time flood detection capability of VNG Flood V1.0 and the quality of VIIRS flood product.

4.2.3. Validation with Landsat-8 OLI imagery

Landsat-8 OLI imagery is a good data source to validate the VIIRS flood product. The validation is performed in two ways: 1) overlapping the VIIRS flood products onto Landsat-8 OLI images at a 30-m resolution; and 2) degrading the Landsat-8 OLI images to a 375-m resolution for a comparison with the VIIRS flood products. The first method can be done via SSEC's Real Earth (<http://realearth.ssec.wisc.edu/>) visualization tool. Here, the near real-time availability of both the VIIRS flood products and the Landsat-8 OLI images in the web browser interface makes it easy to overlap the products and imagery. More than 50 Landsat-8 OLI images have been utilized for validation since 2015 in the USA, and the results are quite promising. Fig. 10 presents an example for Texas on 06 June 2016. Fig. 11(a) is a Landsat-8 OLI image acquired at 16:50 (UTC), wherein the dark blue areas are floodwater. The VNG flood map from 19:43 (UTC) is an overlay on top of the OLI image in Fig. 11(b). From Fig. 11, although the cloud conditions are slightly different between the two observations, over clear-sky regions,

Table 1
Comparison between MODIS flood product and VIIRS flood product.

	Dates	Composition	N_{total}	N_t	N_u	P_f (%)	P_t (%)	P_o (%)
MODIS	11 Jan.	Near real-time	135,797	28,602	8286	78.94	19.85	22.46
		2-day composite	22,384	16,732	20,156	25.25	39.33	54.64
		3-day composite	1435	1129	35,759	21.32	3.04	96.94
	13 Jan.	2-day composite	34,387	24,362	16,982	29.15	47.43	41.07
VIIRS	11 Jan.	3-day composite	29,572	24,298	17,571	17.83	51.54	41.97
		Near real-time	25,258	23,773	4257	5.88	80.55	15.19
	13 Jan.	Near real-time	42,499	41,290	23	2.84	97.10	0.06

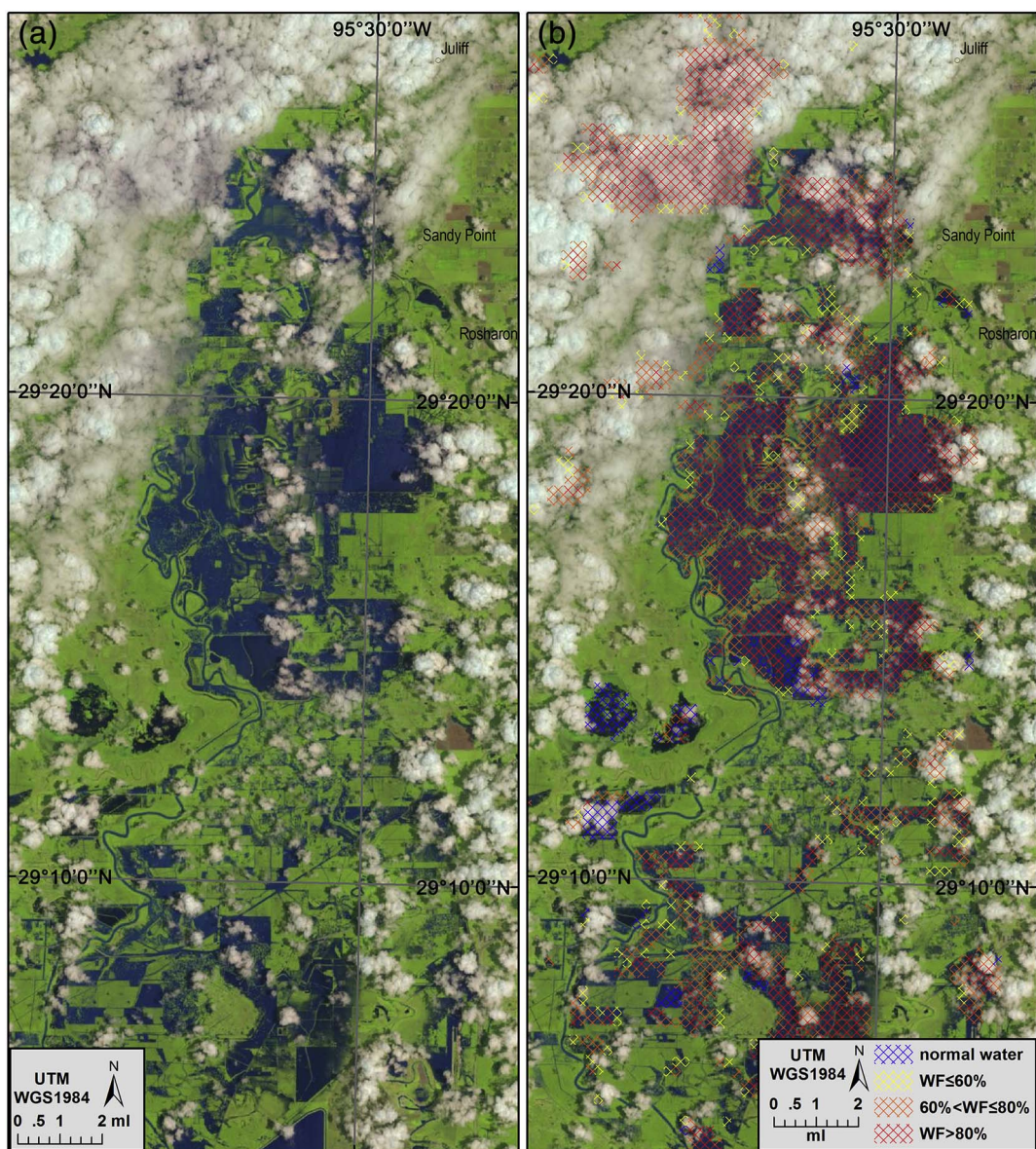


Fig. 11. (a) Landsat-8 OLI false-color composite image in Texas, USA on 06 June 2016 at 16:50 (UTC); (b) VIIRS flood detection map on 06 June 2016 at 19:43 (UTC) overlaid on top of the OLI image from Fig. 10(a).

the VIIRS flood detection results over clear-sky regions were consistent with those of the Landsat-8 OLI imagery. VNG Flood V1.0 accurately detected the most floodwater with larger water fractions (i.e., more red) in the VIIRS flood map corresponding to more floodwaters (i.e., more dark blue) in the Landsat-8 image. This type of performance is typical for other Landsat/SNPP validation comparisons.

To provide a quantitative validation, the Landsat images are remapped to a 375-m resolution for a comparison with the VIIRS flood maps. The comparisons are limited due to numerous differences, including those pertaining to the image modeling, calibration, geolocation accuracy for satellite images at different spatial resolutions, viewing geometry, and overpass times (Schroeder et al., 2008; Li et al., 2012). More than 10 Landsat 30-m images were remapped to spatially match with the VIIRS flood detection results. Cases were selected to include supra-veg/bare soil floods and supra-snow/ice floods. In the Landsat images, water was extracted interactively to generate 30-m water masks, after which the water fractions were calculated in 375-m grids to compare them against the VIIRS water fraction maps. Fig. 12 presents three pairs of flood maps containing pairs of 375-m remapped Landsat flood maps and VIIRS flood maps. Fig. 12(a) is a resampled

Landsat-7 ETM 375-m water fraction map on 13 Jan. 2013 in the Sacramento Valley of California, USA, and its corresponding SNPP/VIIRS flood map is shown in Fig. 12(b). Fig. 12(c) and Fig. 12(d) represent another pair of flood maps from Landsat-7 ETM (Fig. 12(c)) and SNPP/VIIRS (Fig. 12(d)) data on 13 Jan. 2017 in California. Fig. 12(e) presents a 375-m water fraction map from Landsat-8 OLI on 01 April 2015 along the Sag River in northern Alaska, USA, and the SNPP/VIIRS flood map on the same in the same region is shown in Fig. 12(f). From Fig. 12, the VIIRS flood maps show a similar floodwater distribution with the Landsat flood maps, especially in regions with large water fractions. However, there are more small-water-fraction floodwater locations in the Landsat flood maps than in the VIIRS flood maps. This is reasonable because the signals from land are much stronger than those from water when the water fraction is small. Mixed water pixels in the VIIRS imagery exhibit a smaller signal than in the Landsat imagery due to the imager resolution, and it is therefore expected that the VIIRS—or any imager with a similar spatial resolution—would have difficulty detecting mixed water pixels with low water fractions. Another issue is that, around pixels with large water fractions, the VIIRS water fraction retrieval shows larger results than those of the Landsat data. This

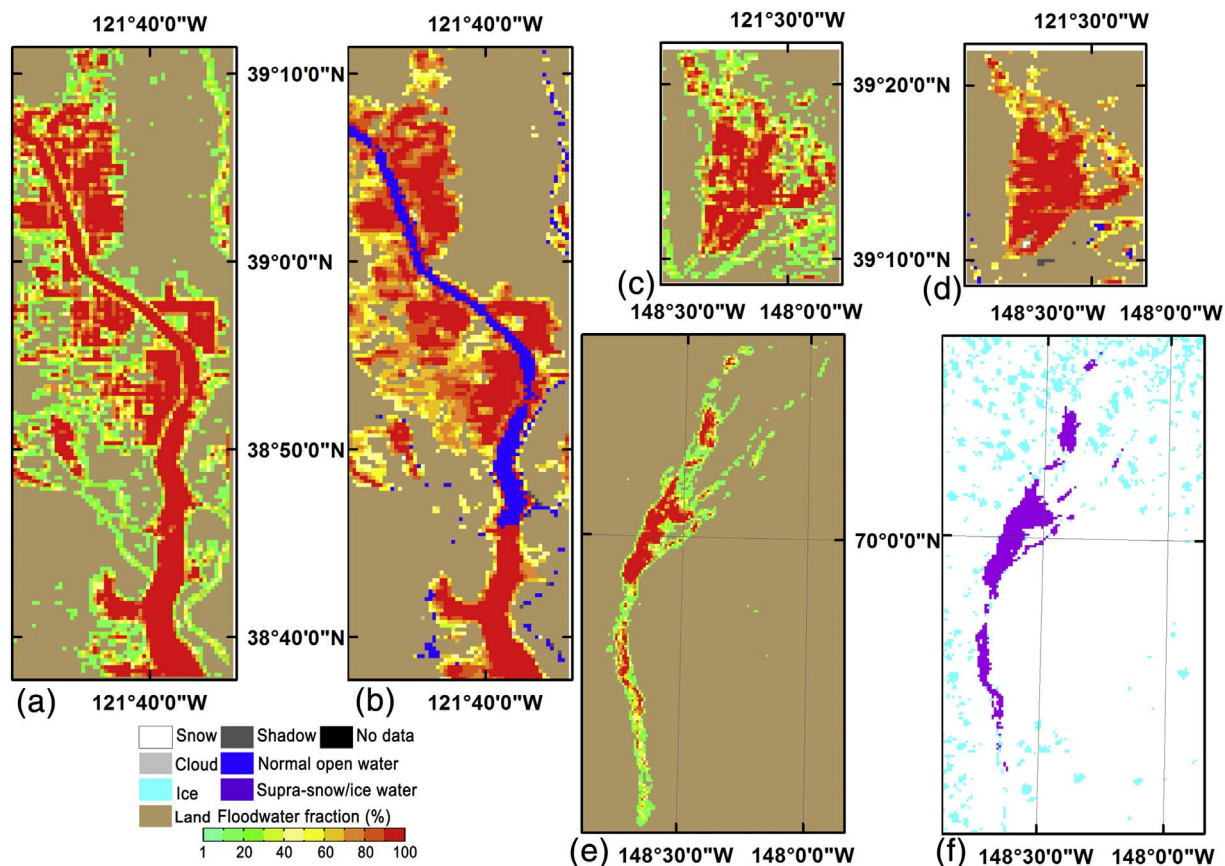


Fig. 12. Three pairs of flood maps for comparison between SNPP/VIIRS and Landsat imagery: (a) Landsat-7 ETM on 13 Jan. 2017 in California, USA, (b) the correspondent SNPP/VIIRS flood map of (a); (c) Landsat-7 ETM on 13 Jan. 2017 in California, USA, (d) the correspondent SNPP/VIIRS flood map of (c); (e) Landsat-8 OLI on 01 April 2015 along the Sag River in Alaska, USA, (f) the correspondent SNPP/VIIRS flood map of (e).

difference may be caused by the difference between the VIIRS and Landsat in their image modeling, geolocation accuracy and viewing geometry.

For further validation, $|D_{WF}|$, which is defined as the absolute water fraction difference between the Landsat and VIIRS data, is calculated, and the statistics of the percentages of $|D_{WF}|$ with different ranges are applied to reflect the detection and retrieval accuracies. For supra-veg/bare soil floodwater, the percentages are calculated in three types: 1) $|D_{WF}| < 100\%$; 2) $|D_{WF}| < 30\%$; 3) $|D_{WF}| < 20\%$. The first type actually ignores the water fraction difference between the Landsat and VIIRS data, and thus, it reflects the water detection accuracy; meanwhile, the other two types indicate the water fraction retrieval accuracy. For supra-snow/ice water without the water fraction retrieval, only the first type is calculated to derive the general detection accuracy. Approximately 50,000 valid samples were collected for supra-veg/bare soil floodwaters and 10,000 samples for supra-snow/ice water from approximately 10 Landsat images and VIIRS flood maps. Fig. 13 presents the validation results of the supra-veg/bare soil water detection, and the results of the supra-snow/ice water detection are shown in Fig. 14. From Fig. 13 and Fig. 14, the water detection and fraction retrieval accuracies increase with the water fraction, which is consistent with the results shown in Fig. 12 with a higher consistency over larger water fractions. For supra-veg/bare soil water, and for water fractions larger than 80%, the detection accuracy is approximately 95%, the water fraction retrieval accuracy with a $|D_{WF}| < 30\%$ is above 90%, and the water fraction retrieval accuracy with a $|D_{WF}| < 20\%$ is above 80%. When the water fractions are below 40%, the water detection accuracy is much higher than the water fraction retrieval accuracy, which somehow reflects that there are more uncertainties in the DNNS method for the water fraction retrieval over

smaller-water-fraction pixels. The detection percentage of supra-snow/ice water reaches approximately 80% when the water fractions are above 80%, and it increases more linearly with the water fraction than supra-veg/bare soil water detection. Overall, the percentages of the supra-snow/ice water detection are approximately 20% less than the supra-veg/bare soil water detection accuracy. This might be related to the higher reflectance of snow/ice surfaces than those of vegetation and bare soils in visible to near infrared channels. The stronger signals of snow/ice surfaces may bring about larger uncertainties in the detection of supra-snow/ice water.

5. Discussion

With the support from JPSS/PGRR Program, VNG Flood V1.0 has been developed for automatic near real-time flood detection using SNPP/VIIRS data. Algorithms include water detection, cloud shadow removal, terrain shadow removal, minor flood detection, water fraction retrieval, and flood determination. With a demonstration project initialized by JPSS/PGRR Program, the software has been running routinely using direct broadcast VIIRS data in near real-time flood detection for five river forecast centers in the USA since 2014. The near real-time flood products are available in SSEC's Real Earth and NOAA's (National Oceanic and Atmospheric Administration) AWIPS-II, and have been carefully evaluated by river forecasters using aerial images and hydrologic observations. Offline evaluation is also done using VIIRS false-color images, MODIS automatic flood maps and Landsat imagery. The near real-time flood detection software has received a positive reception and increasing attention from end-users.

Although VNG Flood V1.0 shows robust performance in flood automation, there are still some limitations and problems with the

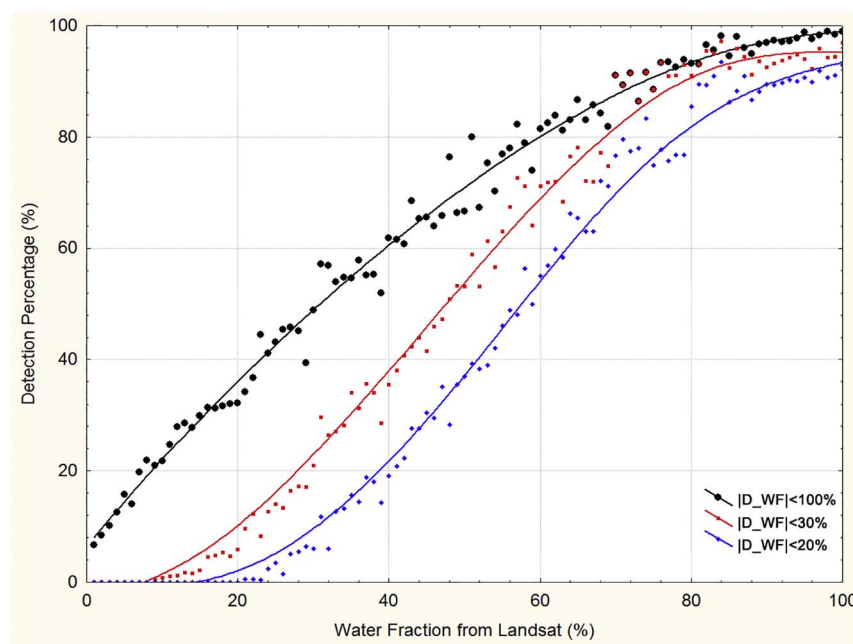


Fig. 13. Scatter plot of supra-veg/bare soil water detection percentage of VIIRS over water fractions from Landsat imagery.

current VIIRS flood products. Cloud cover is the main limitation that sometimes prevents SNPP/VIIRS imagery from obtaining continuous flood observations. This is very common in detecting floods caused by intensive rainfall, when cloud cover may last for an extended period. Persistent cloud coverage may result in severe flood product latency and can be a limiting factor in flood prediction and early warning. The accuracy of cloud detection may also affect the omission ratio of VIIRS flood product. Additionally, flash floods are not tracked well by the product. For flood extent investigation, cloud cover may also be an obstacle from deriving of maximal flood coverage from a single flood map and thus requires multiple-day maximal flood-extent composition process.

The second problem is from cloud shadows. Most cloud shadows are removed from VIIRS flood maps. However, cloud shadows cast by some optically thin clouds may remain in the maps due to the uncertainty of cloud detection and underestimation of cloud heights, which is the

primary error source of flood detection. For more accurate cloud shadow removal, VIIRS cloud type and cloud height products may be considered in future software iterations.

The third problem comes from water fraction retrieval. Although the DNNS method shows good performance in supra-veg/bare soil water fraction retrieval, the validation analysis has shown that there is more uncertainty in water fraction retrieval on small-fraction water pixels than on large-fraction ones. Pixels with wet soil background may result in a larger water fraction retrievals bias, while pixels contaminated by sun glint or thin clouds may result in a low water fraction bias. Additional processing steps may be required for more robust water fraction retrieval over all conditions.

The minor flood detection helps detect many minor to moderate floods in VIIRS flood maps. Soaked soils around rivers/lakes sometimes are counted as floodwaters due to lower reflectance than the surrounding land in visible, near infrared, and short-wave infrared

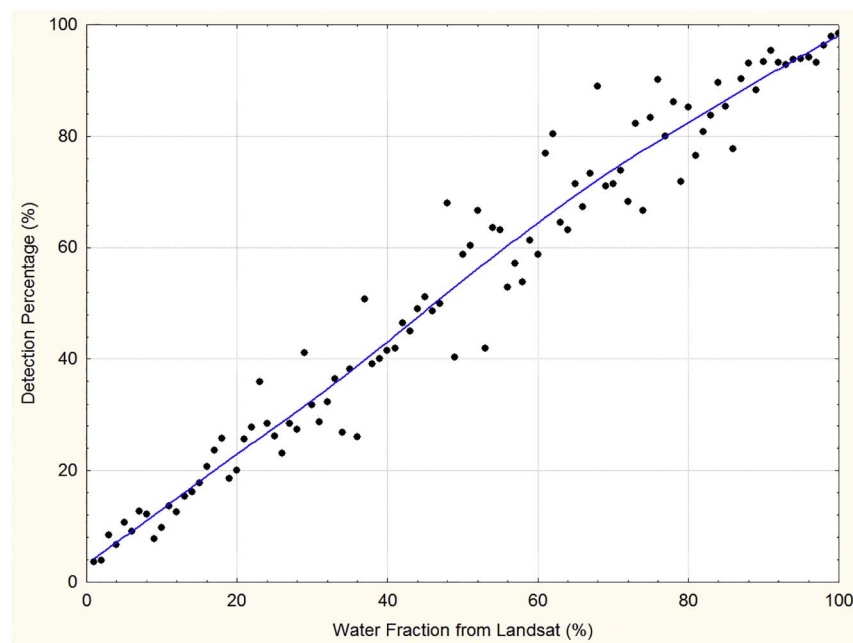


Fig. 14. Scatter plot of supra-snow/ice water detection percentage of VIIRS over water fractions from Landsat imagery.

channels. This is common along coastlines after tides retreat and the wet beach is detected as floodwater in VIIRS flood maps. Further, the method is limited when floodwaters are partially veiled by vegetation cover or urban landscapes.

Despite the limitations in the current flood detection algorithms, the developed VNG Flood V1.0 is still a useful tool for optical-satellite-based flood detection. With several challenges solved, the software shows promising performance in near real-time flood detection. The software has also laid a solid foundation to the work in the next stage. Based on 375-m floodwater fraction product, additional interesting work can be done to obtain more information on floodwater surface levels and depth. The spatial resolution of flood maps can be enhanced from the current 375 m to 30 m or even 10 m with high-resolution DEM data, which provides much more inundation detail than the current 375-m flood maps (Li et al., 2013a). Future capabilities will be incorporated into the second generation VNG Flood V2.0 that will generate 3-D floodwater maps using SNPP/VIIRS imagery.

6. Conclusion

This study presents a comprehensive introduction to VNG Flood V1.0, and can be summarized as follows:

1. The VIIRS NOAA/GMU Flood Version 1.0 software has been developed for automatic near real-time flood detection using SNPP/VIIRS imagery. Floods are divided into two types: supra-veg/bare soil floods and supra-snow/ice floods. A series of algorithms, including water detection, cloud shadow removal, terrain shadow removal, minor flood detection, water fraction retrieval, and floodwater determination, have been developed and integrated into the software. With several challenges resolved, the software shows a high feasibility for applications in near real-time flood mapping at the product level.
2. The software has been running routinely at the SSEC and GINA using direct broadcast VIIRS data to generate near real-time flood maps for the National Weather Service River Forecast Centers in the USA since 2014. These flood maps have been reviewed by river forecasters and applied towards flood operations. Their applications to flood extent monitoring and snowmelt and ice-jam flood predictions have been demonstrated.
3. An evaluation analysis confirms the robust performance of VNG Flood V1.0. The visual inspection, inter-comparison with MODIS flood products, and quantitative validation using Landsat imagery have all shown satisfactory performance.

Acknowledgement

This work was supported by NOAA grant #NA14NES4400007. We thank the five river forecast centers: NCRFC, MBRFC, NERFC, WGRFC and APRFC in the USA for the great efforts they have made to improve this software. The manuscript's contents are solely the opinions of the authors and do not constitute a statement of policy, decision, or position on behalf of NOAA or the U. S. A.

References

- Ali, A., 1989. Study of river flood hydrology in Bangladesh with AVHRR data. *Int. J. Remote Sens.* 10, 1873–1892.
- Andrimont, R.D., Pekel, J.F., Bartholomé, E., Defourny, P., 2012. 8 years water bodies monitoring analysis using MODIS over the African continent. *EGU General Assembly 2012*, 12905.
- Barton, I.J., Bathols, J.M., 1989. Monitoring floods with AVHRR. *Remote Sens. Environ.* 30, 89–94.
- Brakenridge, G.R., 2011. Technical Description, DFO-GSFC Surface Water Mapping Algorithm. <http://floodobservatory.colorado.edu/Tech.html>.
- Brakenridge, G.R., Anderson, E., 2006. MODIS-based flood detection, mapping and measurement: the potential for operational hydrological applications. *Earth Environ. Sci.* 72, 1–12.
- Brakenridge, G.R., Knox, J.C., Paylor, E.D., Magilligan, F.J., 1994. Radar remote sensing aids study of the great flood of 1993. *Eos Trans. AGU* 75 (45), 521–527.
- Carroll, M., Townshend, J., DiMiceli, C., Noojipady, P., Sohlberg, R., 2009. A new global raster water mask at 250 meter resolution. *International Journal of Digital Earth* 2 (4).
- Ceccato, P., Flasse, S., Gregoire, J.M., 2002. Designing a spectral index to estimate vegetation water content from remote sensing data: part 2. Validation and applications. *Remote Sens. Environ.* 82, 198–207.
- Fisher, Adrian, Flood, Neil, Danaher, Tim, 2016. Comparing Landsat water index methods for automated water classification in eastern Australia. *Remote Sens. Environ.* 175, 167–182.
- Gao, B.C., 1996. NDWI—a normalized difference water index for remote sensing of vegetation liquid water from space. *Remote Sens. Environ.* 58 (1996), 257–266.
- Gumley, L.E., King, M.D., 1995. Remote sensing of flooding in the U.S. upper midwest during the summer of 1993. *Bull. Am. Meteorol. Soc.* 76, 6.
- Gupta, R.P., Banerji, S., 1985. Monitoring of reservoir volume using Landsat data. *J. Hydrol.* 77, 159–170.
- Gupta, R.P., Bodechtel, J., 1982. Geotechnical applications of Landsat image analysis of Bhakra dam reservoir, India. *Remote Sens. Environ.* 12, 3–13.
- Hirabayashi, Y., Kanae, S., Emori, S., Oki, T., Kimoto, 2008. Global projections of changing risks of floods and droughts in a changing climate. *Hydrolog. Sci. J.* 53, 754–772.
- Huang, C., Chen, Y., Wu, J., 2014. Mapping spatio-temporal flood inundation dynamics at large river basin scale using time-series flow data and MODIS imagery. *Int. J. Appl. Earth Obs. Geoinf.* 26, 350–362.
- Hutchison, K.D., Mahoney, R.L., Vermont, E.F., Kopp, T.J., Jackson, J.M., Sei, A., Iisager, B.D., 2009. A Geometry-Based Approach to Identifying Cloud Shadows in the VIIRS Cloud Mask Algorithm for NPOESS. *J. Atmos. Ocean. Technol.* 26, 1388–1397.
- Johansson, A.M., Brown, I.A., 2013. Adaptive classification of supraglacial lakes on the West Greenland ice sheet. *IEEE Journal of Select Topics Appl. Earth Obs. Remote. Sens.* 6 (4), 1998–2007. <http://dx.doi.org/10.1109/JSTARS.2012.2233722>.
- Khlopenkov, K.V., Trishchenko, A.P., 2007. New cloud, snow, and cloud shadow detection scheme for historical 1-km AVHRR data over Canada. *J. Atmos. Ocean. Technol.* 24, 322–343.
- Lehner, B., Döll, P., Alcamo, J., Henrichs, T., Kaspar, F., 2006. Estimating the impact of global change on flood and drought risks in Europe: a continental, integrated analysis. *Clim. Chang.* 75, 273–299.
- Lesson, A., Leeson, A., Shepherd, A., Sundal, A.V., Johansson, A.M., Selmes, N., Briggs, K., Hogg, A.E., Fettweis, X., 2013. A comparison of supraglacial lake observations derived from MODIS imagery at the western margin of the Greenland ice sheet. *J. Glaciol.* 59 (218).
- Li, S., Sun, D.L., 2013. Development of an integrated high resolution flood product with multi-source data. In: UMI Dissertations Publishing 2013, (ISBN: 9781303635939, <http://search.proquest.com/docview/1492669000>, 2013).
- Li, S., Sun, D.L., Yu, Y.Y., Csizsar, I., Stefanidis, A., Goldberg, M.D., 2012. A new short-wave infrared (SWIR) method for quantitative water fraction derivation and evaluation with EOS/MODIS and landsat/TM data. *IEEE Trans. Geosci. Remote Sens.* 99.
- Li, S., Sun, D.L., Goldberg, M.D., Stefanidis, A., 2013a. Derivation of 30-m-resolution Water Maps from TERRA/MODIS and SRTM. *Remote Sens. Environ.* 134 (2013), 417–430.
- Li, S., Sun, D.L., Yu, Y.Y., 2013b. Automatic cloud-shadow removal from flood/standing water maps using MSG/SEVIRI imagery. *Int. J. Remote Sens.* 34 (15), 5487–5502.
- Li, S., Sun, D.L., Goldberg, M.D., Sjoberg, B., 2015. Object-based Automatic Terrain Shadow Removal from SNPP/VIIRS Flood Maps. *Int. J. Remote Sens.* 36 (21), 5504–5522.
- Liang, Y.-L., Colgan, W., Lv, Q., Steffen, K., Abdalati, W., Stroeve, J., Gallaher, D., Bayou, N., 2012. A decadal investigation of supraglacial lakes in West Greenland using a fully automatic detection and tracking algorithm. *Remote Sens. Environ.* 123, 127–138 August 2012.
- Liu, Y., Maidment, D.R., Tarboton, D.G., Zheng, X., Yildirim, A., Sazib, N.S., Wang, S.W., 2016. A CyberGIS approach to generating high-resolution height above nearest drainage (HAND) raster for national flood mapping. *CyberGIS Center Technical Report 2016*.
- Martinis, S., Twete, A., Voigt, S., 2009. Towards operational near real-time flood detection using a split-based automatic thresholding procedure on high resolution TerraSAR-X data. *Nat. Hazards Earth Syst. Sci.* 9, 303–314. <http://dx.doi.org/10.5194/nhess-9-303-2009>.
- Martinis, S., Twete, A., Strobl, C., Kersten, J., Stein, E., 2013. A Multi-Scale Flood Monitoring System Based on Fully Automatic MODIS and TerraSAR-X Processing Chains. *Remote Sens.* 5, 5598–5619.
- Matgen, P., Schumann, G., Henryc, J.-B., Hoffmann, L., Pfistera, L., 2007. Integration of SAR-derived river inundation areas, high-precision topographic data and a river flow model toward near real-time flood management. *Int. J. Appl. Earth Obs. Geoinf.* 9, 247–263.
- Matgen, P., Hostache, R., Schumann, G., Pfister, L., Hoffmann, L., Savenije, H., 2011. Towards an automated SAR-based flood monitoring system: lessons learned from two case studies. *Phys. Chem. Earth* 36, 241–252.
- Milly, P., Wetherald, R., Dunne, K., Delworth, T., 2002. Increasing risk of great floods in a changing climate. *Nature* 415, 514–517.
- Mueller, N., Lewis, A., Roberts, D., Ring, S., Melrose, R., Sixsmith, J., Lym-Burner, L., McIntyre, A., Tan, P., Curnow, S., and Ip, A., 2016. Water observations from space: Mapping surface water from 25 years of Landsat imagery across Australia. *Remote Sens. Environ.* 174, 341–352.
- Pulvirenti, L., Pierdicca, N., Chini, M., Guerrero, L., 2011. An algorithm for operational flood mapping from Synthetic Aperture Radar (SAR) data using fuzzy logic. *Nat. Hazards Earth Syst. Sci.* 11, 529–540. <http://dx.doi.org/10.5194/nhess-11-529-2011>.

- Rabus, B., Eineder, M., Roth, A., Bamler, R., 2003. The shuttle radar topography mission – a new class of digital elevation models acquired by spaceborne radar. *Int. Arch. Photogramm. Remote. Sens. Spat. Inf. Sci.* 57, 241–262.
- Rouse, J.W., Haas, R.H., Scheel, J.A., Deering, D.W., 1974. Monitoring vegetation systems in the great plains with ERTS. In: Proceedings, 3rd Earth Resource Technology Satellite (ERTS) Symposium. Vol. 1. pp. 48–62.
- Schroeder, W., Prins, E., Giglio, L., Csizsar, I., Schmidt, C., Morisette, J., Morton, D., 2008. Validation of GOES and MODIS active fire detection products using ASTER and ETM + data. *Remote Sens. Environ.* 112 (2008), 2711–2726.
- Schumann, G., Hostache, R., Puech, C., Hoffmann, L., Matgen, P., Pappenberger, F., Pfister, L., 2007. High-Resolution 3-D Flood Information From Radar Imagery for Flood Hazard Management. *IEEE Trans. Geosci. Remote Sens.* 45, 1715–1725.
- Sellers, P.J., 1985. Canopy reflectance, photosynthesis, and transpiration. *Int. J. Remote Sens.* 6, 1335–1372.
- Sheng, Y., Gong, P., 2001. Quantitative dynamic flood monitoring with NOAA AVHRR. *Int. J. Remote Sens.* 22 (9), 1709–1724.
- Sheng, Y., Xiao, Q., 1994. Water identification in cloud-contaminated NOAA/AVHRR imagery. *Remote Sens. Environ.* 9, 247–255.
- Sheng, Y., Su, Y., Xiao, Q., 1998. Challenging the cloud-contamination problem in flood monitoring with NOAA/AVHRR imagery. *Photogramm. Eng. Remote. Sens.* 64, 191–198.
- Shepard, M.K., Campbell, B.A., Bulmer, M.H., Farr, T.G., Gaddis, L.R., Plaut, J.J., 2001. The roughness of natural terrain: A planetary and remote sensing perspective. *J. Geophys. Res.* 106 (E12), 32,777–32,795.
- Sun, D.L., Yu, Y.Y., Zhang, R., Li, S., Goldberg, M.D., 2012. Towards Operational Automatic Flood Detection Using EOS/MODIS data. *Photogramm. Eng. Remote. Sens.* 78 (6), 637–646.
- Tachikawa, T., Hato, M., Kaku, M., Iwasaki, A., 2011. The Characteristics of ASTER GDEM Version 2. IGARSS (July 2011).
- Thompson, R.J., Oosterom, P.V., Zlatanova, S., Giesen, N.V.D., Goulevitch, B., 2011. Monitoring the Extent of flooding – based on a case study in queensland, the international archives of the photogrammetry. *Int. Arch. Photogramm. Remote. Sens. Spat. Inf. Sci.* 34 (Part XXX).
- Ticehurst, C., Guerschman, J.P., Chen, Y., 2014. The strengths and limitations in using the daily MODIS open water likelihood algorithm for identifying flood events. *Remote Sens.* 6 (12), 11791–11809.
- Ticehurst, C., Dutta, D., Karim, F., Petheram, C., Guerschman, J.P., 2015. Improving the accuracy of daily MODIS OWL flood inundation mapping using hydrodynamic modelling. *Nat. Hazards* 78 (2), 803–820.
- Tsugawa, R., James, B., 2011. Joint polar satellite system (JPSS) VIIRS snow cover algorithm theoretical basis document. In: NPOESS Common Data Format Control Book – External Volume 5 Metadata, D34862-05.
- Tulbure, M.G., Broich, M., Stehman, S.V., Kommareddy, A., 2016. Surface water extent dynamics from three decades of seasonally continuous Landsat time series at sub-continental scale in a semi-arid region. *Remote Sens. Environ.* 178, 142–157.
- Wang, Y., Colby, J.D., Mulcahy, K.A., 2002. An efficient method for mapping flood extent in a coastal floodplain using Landsat TM and DEM data. *Int. J. Remote Sens.* 23 (18), 3681–3696.
- Wiesnet, D.R., McGinnis, D.V., Pritchard, J.A., 1974. Mapping of the 1973 Mississippi river floods by the NOAA-2 Satellite. *Water Resour. Bull.* 10 (5), 1040–1049.
- Xian, G., Homer, C., Fry, J., 2009. Updating the 2001 National Land Cover Database land cover classification to 2006 by using Landsat imagery change detection methods. *Remote Sens. Environ.* 113, 1133–1147.
- Xiao, X.G., Shen, Z.X., Qin, X.G., 2001. Assessing the potential of vegetation sensor data for mapping snow and ice cover: a normalized difference snow and ice index. *Int. J. Remote Sens.* 22 (13), 2479–2487.
- Zhang, Y.X., Zhang, L.J., Huang, Y.F., Rong, Z.G., Hu, X.Q., Liu, J.J., Zhang, G.S., 2008. Spectral Data Sets for Satellite Calibration Site and Typical Earth Objects. M., China Meteorological Press (ISBN: 978-7-5029-4422-3).